

Hot Schrödinger Cat States

Ian Yang^{1,2,†}, Thomas Agrenius^{2,3,†}, Vasilisa Usova^{1,2}, Oriol Romero-Isart^{2,3,*},
Gerhard Kirchmair^{1,2,**}

¹Institute for Experimental Physics, University of Innsbruck, 6020 Innsbruck, Austria

²Institute for Quantum Optics and Quantum Information, Austrian Academy of Sciences, 6020 Innsbruck, Austria

³Institute for Theoretical Physics, University of Innsbruck, 6020 Innsbruck, Austria

*Present address: ICFO - Institut de Ciències Fotoniques, The Barcelona Institute of Science and Technology, Castelldefels (Barcelona) 08860, Spain and ICREA, Passeig Lluís Companys 23, 08010, Barcelona, Spain

**To whom correspondence should be addressed; E-mail: gerhard.kirchmair@uibk.ac.at

The observation of quantum phenomena often necessitates sufficiently pure states, a requirement that can be challenging to achieve. In this study, our goal is to prepare a non-classical state originating from a mixed state, utilizing dynamics that preserve the initial low purity of the state. We generate a quantum superposition of displaced thermal states within a microwave cavity using only unitary interactions with a transmon qubit. We measure the Wigner functions of these “hot” Schrödinger cat states for an initial purity as low as 0.06. This corresponds to a cavity mode temperature of up to 1.8 Kelvin, sixty times hotter than the cavity’s physical environment. Our realization of highly mixed quantum superposition states could be implemented with other continuous-variable systems e.g. nanomechanical oscillators, for which ground-state cooling remains challenging.

The quantum superposition principle allows us to prepare a system in a superposition of two arbitrary states. The paradigmatic example is the superposition of two coherent states, which are pure states with Heisenberg-limited quantum fluctuations [1]. While the superposition of coherent states is typically called a Schrödinger cat state, in Schrödinger’s original thought experiment, the cat — a body-temperature and out-of-equilibrium system — is prepared in a superposition of two mixed states dominated by classical fluctuations [2].

Experimental demonstrations of Schrödinger cat states typically focus on a continuous-variable degree of freedom, such as the one-dimensional motion of a particle in a harmonic potential [3] or a single electromagnetic field mode in a cavity [4]. The cat states are usually prepared by applying a given “cat state protocol” to an initial vacuum Fock state $\hat{\rho}_0 = |0\rangle\langle 0|$, created by cooling the system to its ground state. This results in a pure quantum state which can be written as $|\alpha\rangle + e^{i\phi}|\alpha\rangle$, where $|\pm\alpha\rangle$ are coherent states of the continuous-variable system with complex amplitude α and relative phase ϕ . We hereafter call this a “cold” Schrödinger cat state. It has an emblematic Wigner

function exhibiting an interference pattern, see Figure 1A.

One could ask what type of state would be prepared if the same “cat state protocol” is applied to an initial thermal state $\hat{\rho}_T$ with a finite average thermal excitation number n_{th} [5–10]. Would these “hot” Schrödinger cat states exhibit quantum features given that (i) the purity of the initial state $\mathcal{P} = \text{tr}[\hat{\rho}_T^2] = 1/(2n_{\text{th}} + 1)$ is significantly less than one for large n_{th} , and (ii) we consider “cat state protocols” that do not remove entropy from the system? In other words, can a highly mixed state exhibit unambiguous quantum features?

In this article, we experimentally show that indeed, these “hot” Schrödinger cat states exhibit quantum features despite being highly mixed. More precisely, we implement two unitary protocols, previously used to prepare cold cats [11, 12], on initial states with a nonzero n_{th} . We vary n_{th} of the initial states up to 7.6(2) (corresponding to $\mathcal{P} = 0.062(2)$) and perform direct Wigner function measurements on the final states. The created “hot” Schrödinger cat states show Wigner-negative interference patterns for all investigated values of n_{th} in the initial state (Figure 1B-G).

Our experimental platform is a circuit quantum electrodynamics (cQED) setup [13]. The “hot” cat states are prepared in a microwave cavity mode, which is well-described as a quantum harmonic oscillator. The cavity mode is coupled to a two-level system which is used to prepare the cat states. The setup is placed inside a dilution refrigerator and cooled to a temperature of 30 mK (see Figure S1 for the full experimental schematic). The cavity is a high-coherence $\lambda/4$ post cavity, made up of high-purity niobium, with a resonance frequency $\omega_c/2\pi = 4.545$ GHz [14], and a relaxation time $T_{1,c} = 110(2)$ μ s. For the two-level system, we use a transmon qubit with a resonance frequency $\omega_q/2\pi = 5.735$ GHz, qubit lifetime $T_1 = 31.0(4)$ μ s, and coherence time $T_2^* = 12.5(4)$ μ s. The cavity-qubit interaction is dispersive with the dominant Hamiltonian term $\hat{H} = -\hbar\chi_{qc}\hat{c}^\dagger\hat{c}|e\rangle\langle e|$. Here, \hat{c}^\dagger and \hat{c} are the cavity mode creation and annihilation operators, $|e\rangle$ is the excited state of the qubit, $\chi_{qc}/2\pi = 1.499(3)$ MHz is the dispersive shift, and \hbar is the reduced Planck’s constant. Qubit state measurements are performed through an additional dispersively coupled microstrip resonator with frequency $\omega_r/2\pi = 7.534$ GHz. This setup allows for direct measurements of the cavity Wigner function $W(\beta) \equiv 2 \text{Tr} [\hat{D}(\beta)\hat{H}\hat{D}^\dagger(\beta)]/\pi$ [15]. Here β is a complex parameter, $\hat{D}(\beta)$ is the cavity displacement operator, and \hat{H} is the cavity parity operator [16]. We calibrate the Wigner function measurement by preparing a single photon Fock state in the cavity (Figure S2).

The thermal initial state of the cavity mode, hotter than its environment, is created by equilibrating the cavity mode with a heat bath in the form of filtered and amplified Johnson-Nyquist noise from a 50 Ω resistor. The heat bath is then disconnected (to prevent it from causing additional decoherence) and the cat state preparation commences immediately [17]. The state preparation and measurement protocols take up to 1.9 μ s which is much faster than the cavity relaxation time $T_{1,c}$. Thus, there is neither cooling nor heating of the cavity mode during the protocols. To verify that the produced initial state is thermal, we characterize the photon statistics of the cavity state with the added noise via qubit spectroscopy [18], which also allows us to relate the noise power to n_{th} (Figure S4).

The two protocols used to prepare the hot cat states from the thermal initial state are adaptations of two protocols known in the cQED community as the echoed conditional displacement (ECD) [11] and qcMAP [12]

protocols. The quantum circuit diagrams for the protocols we use are shown in Figure 2A. To illustrate the state generation, we decompose the initial thermal state in a basis of cavity coherent states $|\gamma\rangle = \hat{D}(\gamma)|0\rangle$ with γ a complex parameter [1]. We can then discuss the action of the protocols on the state $|\gamma\rangle|g\rangle$, where $|g\rangle$ is the qubit ground state. The first operation sequence prepares the qubit in the superposition state $|g\rangle + e^{i\phi}|e\rangle$, where ϕ is a controllable phase shift, and the cavity in the displaced state $|\gamma + \alpha\rangle$ [19]. Next, the cavity-qubit state becomes entangled through time evolution under the dispersive interaction \hat{H} , as illustrated in Figure 2B and C for ECD and qcMAP respectively. The qcMAP protocol has an uninterrupted time evolution, while the ECD protocol has additional displacements and a qubit echo pulse inserted at half the evolution time. At the end of the time evolution, we have created the state $e^{i\phi}|i\gamma - \alpha\rangle|g\rangle + |i\gamma + \alpha\rangle|e\rangle$ with the ECD protocol and the state $|\gamma + \alpha\rangle|g\rangle + e^{i\phi}|-\gamma - \alpha\rangle|e\rangle$ with the qcMAP protocol. The final three operations in Figure 2A disentangle the qubit from the cavity. We center the $|e\rangle$ branch with a displacement $-\alpha$ for ECD and α for qcMAP. Next, we apply a qubit π -pulse selective to the $|e\rangle$ branch only. Finally, we invert the previous displacement. The selective π -pulse has a Gaussian envelope with standard deviation in time σ_t . This induces a Fock number-dependent qubit flip probability $P_{g\leftrightarrow e}(n) = \exp\{-(\chi_{qc}\sigma_t n)^2\}$ [20, 21]. We choose σ_t so that this probability is large for the non-displaced thermal state but small for the displaced thermal state (Figure 2D). This requires that α is chosen large enough so that the Fock number distributions of the initial thermal state and the thermal state displaced by 2α do not overlap. In a phase-space picture, we flip the qubit only for phase-space points within a finite radius of the origin (Figure 2E).

We run our experiment with an initial thermal excitation number of $n_{\text{th}} = 0.75(1), 1.44(2), 1.84(3), 3.48(7), 7.6(2)$, corresponding respectively to purities of $\mathcal{P} = 0.400(3), 0.258(3), 0.214(3), 0.126(2), 0.062(2)$. We use $\alpha = 3$, set $\phi = 0$, and use a disentanglement pulse width of $\sigma_t = 20$ ns. Figure 1B,C show Wigner function measurements on a grid of phase-space points β for $n_{\text{th}} = 3.48$. Figure 1D-G show Wigner function measurements along the $\text{Re}\{\beta\}$ and $\text{Im}\{\beta\}$ axes as n_{th} is varied. While the ECD and qcMAP protocols are known to prepare equivalent cold cats, we observe that they lead to distinct outcomes when applied to thermal initial states; compare panels

B and C in Figure 1. In both cases, the Wigner functions have two separated Gaussians centered at α and $-\alpha$, associated with the classical probability distribution of the displaced thermal initial states. Centered between these is an interference pattern of oscillations with negative values, which produces an interference pattern in the marginal distribution along $\text{Im}\{\beta\}$. In the ECD state, the envelope of the interference pattern grows in radius and decreases in amplitude with n_{th} similar to the displaced thermal states themselves (Figure 1D,E). In the qcMAP state, the envelope shrinks with increasing n_{th} , but its amplitude decreases more slowly than the displaced thermal states (Figure 1F,G). The data for all prepared states show clear negative values in the interference pattern regardless of their n_{th} .

These results can be understood as follows. We show in [22] that, under ideal conditions, the ECD and qcMAP protocols are equivalent to the application of two different quantum operators, namely $\hat{S}_1 \equiv [\hat{D}(\alpha) + e^{i\phi}\hat{D}(-\alpha)]/\sqrt{2}$ (ECD) and $\hat{S}_2 \equiv [1 + e^{i\phi}\hat{I}]\hat{D}(\alpha)/\sqrt{2}$ (qcMAP), to the initial state $\hat{\rho}_T$ [23]. The Wigner functions prepared from $\hat{\rho}_T$ by the operators $\hat{S}_{1,2}$ are $W_{1,2}(\beta) \equiv \frac{1}{2} [W_T(\beta - \alpha) + W_T(\beta + \alpha) + C_{1,2}(\beta)]$ where $W_T(\beta \pm \alpha)$ are the Wigner functions of the left- and right-displaced thermal states, and the third term, which represents the quantum superposition property of the state, is different for the two preparations: $C_{1,2}(\beta) = 2 \cos(4\text{Im}\{\alpha^*\beta\} + \phi) f_{1,2}(\beta)$ [24]. For ECD, $f_1(\beta) \equiv W_T(\beta) = 2\mathcal{P}e^{-2\mathcal{P}|\beta|^2}/\pi$ is the thermal initial state. For qcMAP, $f_2(\beta) \equiv 2e^{-2|\beta|^2/\mathcal{P}}/\pi$ is related to the characteristic function [25] of the initial state. We plot examples of $W_{1,2}(\beta)$ in Figure 3A. As illustrated there, when $n_{\text{th}} \rightarrow 0$ ($\mathcal{P} \rightarrow 1$), $f_{1,2}(\beta)$ become identical and $W_{1,2}(\beta)$ both become equal to the cold cat Wigner function. When $n_{\text{th}} > 0$, the phase-space radius of $f_1(\beta)$ grows at the same rate as the phase-space radii of $W_T(\beta \pm \alpha)$, while the phase-space radius of $f_2(\beta)$ shrinks. For both states, the $\text{Im}\{\beta\}$ marginal probability distribution contains interference fringes with period $\pi/2\alpha$ and full contrast independently of n_{th} . We remark that for $\phi = n\pi$ with n integer, $W_2(0)$ is always saturated to the Wigner function upper/lower bounds $\pm 2/\pi$, corresponding to parity values $\langle \hat{I} \rangle = \pm 1$, independently of n_{th} . Realizing this saturation of parity could be useful for hardware-efficient encoding in bosonic qubit states in the presence of finite mode temperature [26, 27].

We gain further understanding of the hot cat

states by using the ideal Wigner functions $W_{1,2}(\beta)$ to compute the coherence function $g(x_1, x_2) \equiv |\langle x_1 | \hat{\rho} | x_2 \rangle| / \sqrt{\langle x_1 | \hat{\rho} | x_1 \rangle \langle x_2 | \hat{\rho} | x_2 \rangle}$ of the hot cat states. Here, $x_{1,2}$ are eigenvalues and $|x_{1,2}\rangle$ eigenkets of the dimensionless quadrature operator $\hat{x} \equiv (\hat{c} + \hat{c}^\dagger)/\sqrt{2}$. The coherence function is upper-bounded as $g(x_1, x_2) \leq 1$, where saturation of the bound implies that full-contrast quantum interference could be observed [28]. The thermal state coherence function is a Gaussian $e^{-|x_1 - x_2|^2/2\xi_{\text{th}}^2}$ where the scale is the coherence length $\xi_{\text{th}} = \sqrt{2\mathcal{P}/(1 - \mathcal{P}^2)} \approx 1/\sqrt{n_{\text{th}}}$. As n_{th} increases, the coherence length shrinks and the coherence function decays faster with $|x_1 - x_2|$ (Figure 3B). The cat state coherence functions computed from $W_{1,2}(\beta)$ can be written $e^{-(|x_1| - |x_2|)^2/2\xi_{\text{th}}^2}$ along the one-dimensional section shown in Figure 3C. Compared to the thermal state, the cat state coherence function has an additional peak at $x_1 = -x_2$ along this section, contributed by the term $C_{1,2}(\beta)$ in $W_{1,2}(\beta)$. The value of n_{th} affects only how narrow this extra peak is, but not its maximum value, which is always saturated to 1 in the ideal case. We present the full two-dimensional coherence functions of the cat states in Figure S5.

We emphasize that the additional peak in the cat state coherence function comes from the action of the cat creation operators $\hat{S}_{1,2}$. These operators thus generate coherence not present in the initial state. The additional coherence function peak is also generated in experiments which observe interference patterns from superpositions of thermal clouds of atoms prepared using Bragg diffraction [29] or Stern-Gerlach interferometry [30]. In contrast, the additional peak is not present in the state obtained by sending a thermal state through a double slit grating (see e.g. [31]), nor in a completely dephased cold cat state, namely $\hat{\rho}_{\text{dephased}} = \frac{1}{2}(|\alpha\rangle\langle\alpha| + |-\alpha\rangle\langle-\alpha|)$ (see e.g. [32]). Note that $\hat{\rho}_{\text{dephased}}$ has purity 1/2 but a completely positive Wigner function ($W_{1,2}(\beta)$ with $C_{1,2}(\beta) = 0$), whereas we experimentally prepare states with negative Wigner functions down to purities of 0.06.

The measured Wigner functions (Figure 1) deviate from the ideal Wigner functions $W_{1,2}(\beta)$ (Figure 3A) mainly due to qubit operation imperfections and perturbative Hamiltonian nonlinearities. We construct an *ab initio* model of the state preparation protocols that includes the nonlinearities, the shape and timings of the qubit pulses, and decoherence (see Figure S6 and Table S1 for the experimental characterisation). We account for the effects of residual cavity-qubit entan-

gement (due to pulse imperfections) in the modelling of the Wigner function measurement. We find that the model reproduces the imperfections seen in the data (Figures S7-S8).

By turning the model features on and off, we attribute each imperfection to a cause (Figures S9-S11). Here, we summarize the conclusions and further details are given in [22]. The leading perturbative Hamiltonian terms $\hat{H}' = -\frac{1}{2}(K_c + \chi'_{qc}|e\rangle\langle e|)\hat{c}^\dagger\hat{c}^\dagger\hat{c}\hat{c}(K_c/2\pi = 4.9(1) \text{ kHz}, \chi'_{qc}/2\pi = 12.8(9) \text{ kHz})$ cause a smearing and bending distortion of the Wigner functions which is similar to that observed in previous experiments [33]. The 20 ns width of the disentanglement pulse causes left-right asymmetries of the displaced thermal states as well as bending distortions of the fringes. In particular, the nonlinearities and finite pulse widths together cause the qcMAP linecuts (Figure 2D) to deviate from those predicted by $W_2(\beta)$, with an n_{th} -dependent reduction of the maximum of $C_2(\beta)$. The extra fringes in the ECD state as compared to theory are caused by instrumentation limitations to the minimum qubit pulse width that we can achieve (Gaussian standard deviation of 6 ns).

We have demonstrated and characterized the preparation of quantum superposition states directly from thermally excited initial states using only unitary dynamics. Preparing “hotter” (larger initial thermal occupation number) cat states requires using larger cavity displacements, where limitations eventually appear due to the finite coherence time and perturbative nonlinearities in our experiment. State-of-the-art setups capable of cold cat states with $\alpha = 32$ were recently reported [34]. Under ideal conditions (including ideal measurement precision), standard quantum-mechanical theory predicts no upper limit on and no loss of contrast due to the thermal occupation number of a hot cat state [5–10].

Hot Schrödinger cat states are in principle realizable in any continuous-variable quantum system. This is particularly relevant for systems where long coherence times have been achieved but ground-state cooling is not (yet) available. Specific examples include nanomechanical systems such as carbon nanotubes [35], and levitated magnetic [36, 37] and electrostatically trapped dielectric particles [38–41].

Acknowledgments

[†] IY and TA contributed equally to this work.

TA and ORI wish to thank Lukas Neumeier for useful discussions. IY, VU and GK wish to thank Johannes Fink for the etching of our Niobium cavities.

Funding: IY, VU and GK were funded in part by the Austrian Science Fund (FWF) DOI 10.55776/F71 and 10.55776/I4395 QuantERA grant QuCOS. For the purpose of open access, the author has applied a CC BY public copyright licence to any Author Accepted Manuscript version arising from this submission. TA and ORI were supported by the European Research Council (ERC) under Grant Agreement No. [951234] (Q-Xtreme ERC-2020-SyG).

Author contributions: IY carried out the experiment with support from VU. TA carried out the theoretical analysis with support from the other authors. The numerical simulations were done by IY, TA, and VU. ORI and GK conceived of and supervised the project. All authors were involved in the writing and the editing of the paper.

Competing interests: The authors declare no competing interests.

Data availability: The data that supports the plots within this paper and the supplementary material will be available via a permanent, public repository, Zenodo.

References

1. Glauber, R. J. Coherent and Incoherent States of the Radiation Field. *Physical Review* **131**, 2766–2788. <https://link.aps.org/doi/10.1103/PhysRev.131.2766> (1963).
2. Schrödinger, E. Die gegenwärtige Situation in der Quantenmechanik. *Naturwissenschaften* **23**, 807–812. <https://doi.org/10.1007/BF01491891> (1935).
3. Monroe, C., Meekhof, D. M., King, B. E. & Wineland, D. J. A “Schrödinger Cat” Superposition State of an Atom. *Science* **272**, 1131–1136. <https://www.science.org/doi/abs/10.1126/science.272.5265.1131> (1996).

4. Brune, M., Hagley, E., Dreyer, J., Maître, X., Maali, A., Wunderlich, C., Raimond, J. M. & Haroche, S. Observing the Progressive Decoherence of the “Meter” in a Quantum Measurement. *Physical Review Letters* **77**, 4887–4890. <https://link.aps.org/doi/10.1103/PhysRevLett.77.4887> (1996).
5. Zhu, K., Tang, H., Li, C., Huang, D., Li, X. & Li, X. The Quantum Statistical Properties of Superposition Coherent States with Thermal Noise. *Journal of Modern Optics* **43**, 323–336. <https://doi.org/10.1080/09500349608232745> (1996).
6. Huyet, G., Franke-Arnold, S. & Barnett, S. M. Superposition States at Finite Temperature. *Physical Review A* **63**, 043812. <https://link.aps.org/doi/10.1103/PhysRevA.63.043812> (2001).
7. Jeong, H. & Ralph, T. C. Transfer of Nonclassical Properties from a Microscopic Superposition to Macroscopic Thermal States in the High Temperature Limit. *Physical Review Letters* **97**, 100401. <https://link.aps.org/doi/10.1103/PhysRevLett.97.100401> (2006).
8. Zheng, S.-B. Macroscopic Superposition and Entanglement for Displaced Thermal Fields Induced by a Single Atom. *Physical Review A* **75**, 032114. <https://link.aps.org/doi/10.1103/PhysRevA.75.032114> (2007).
9. Jeong, H. & Ralph, T. C. Quantum Superpositions and Entanglement of Thermal States at High Temperatures and Their Applications to Quantum-Information Processing. *Physical Review A* **76**, 042103. <https://link.aps.org/doi/10.1103/PhysRevA.76.042103> (2007).
10. Nicacio, F., Maia, R. N. P., Toscano, F. & Vallejos, R. O. Phase Space Structure of Generalized Gaussian Cat States. *Physics Letters A* **374**, 4385–4392. <https://www.sciencedirect.com/science/article/pii/S0375960110011370> (2010).
11. Eickbusch, A., Sivak, V., Ding, A. Z., Elder, S. S., Jha, S. R., Venkatraman, J., Royer, B., Girvin, S. M., Schoelkopf, R. J. & Devoret, M. H. Fast universal control of an oscillator with weak dispersive coupling to a qubit. *Nature Physics* **18**, 1464–1469. <https://www.nature.com/articles/s41567-022-01776-9> (2022).
12. Leghtas, Z., Kirchmair, G., Vlastakis, B., Devoret, M. H., Schoelkopf, R. J. & Mirrahimi, M. Deterministic protocol for mapping a qubit to coherent state superpositions in a cavity. *Physical Review A* **87**, 042315. <https://link.aps.org/doi/10.1103/PhysRevA.87.042315> (2013).
13. Reagor, M., Pfaff, W., Axline, C., Heeres, R. W., Ofek, N., Sliwa, K., Holland, E., Wang, C., Blumoff, J., Chou, K., Hatridge, M. J., Frunzio, L., Devoret, M. H., Jiang, L. & Schoelkopf, R. J. Quantum memory with millisecond coherence in circuit QED. *Physical Review B* **94**, 014506. <https://link.aps.org/doi/10.1103/PhysRevB.94.014506> (2016).
14. Heidler, P., Schneider, C. M. F., Kustura, K., Gonzalez-Ballester, C., Romero-Isart, O. & Kirchmair, G. Non-Markovian Effects of Two-Level Systems in a Niobium Coaxial Resonator with a Single-Photon Lifetime of 10 milliseconds. *Physical Review Applied* **16**, 034024. <https://link.aps.org/doi/10.1103/PhysRevApplied.16.034024> (2021).
15. Vlastakis, B., Kirchmair, G., Leghtas, Z., Nigg, S. E., Frunzio, L., Girvin, S. M., Mirrahimi, M., Devoret, M. H. & Schoelkopf, R. J. Deterministically Encoding Quantum Information Using 100-Photon Schrödinger Cat States. *Science* **342**, 607–610. <https://www.science.org/doi/10.1126/science.1243289> (2013).
16. Royer, A. Wigner Function as the Expectation Value of a Parity Operator. *Physical Review A* **15**, 449–450. <https://link.aps.org/doi/10.1103/PhysRevA.15.449> (1977).
17. In Figure S3, we additionally report results from running the experiment with the heat bath left connected during the entire protocol.
18. Schuster, D. I., Houck, A. A., Schreier, J. A., Wallraff, A., Gambetta, J. M., Blais, A., Frunzio, L., Majer, J., Johnson, B., Devoret, M. H., Girvin, S. M. & Schoelkopf, R. J. Resolving photon number states in a superconducting circuit. *Nature*

- 445, 515–518. <https://www.nature.com/articles/nature05461> (2007).
19. For simplicity of presentation, we ignore normalization, global phases, and we absorb all relative phase shifts into ϕ . In particular, we absorb a geometric phase shift $2|\alpha|^2$ which accumulates during the ECD displacement operations. In the experiment, the geometric phase shift is cancelled via ϕ .
 20. Thomas, G. F. Validity of the Rosen-Zener Conjecture for Gaussian-modulated Pulses. *Physical Review A* **27**, 2744–2746. <https://link.aps.org/doi/10.1103/PhysRevA.27.2744> (1983).
 21. Mihov, I. S. & Vitanov, N. V. *Pulse Shape Effects in Qubit Dynamics Demonstrated on an IBM Quantum Computer* arXiv: 2301.10004. <http://arxiv.org/abs/2301.10004>.
 22. See the Supplemental Materials to this article.
 23. The ECD protocol is more generally equivalent to the operator $\hat{S}'_1 \equiv \hat{S}_1 \Big|_{\phi \rightarrow \phi + 2|\alpha|^2} i^{\hat{c}^\dagger \hat{c}}$, but these differences vanish when the initial state is thermal and the geometric phase is cancelled by ϕ .
 24. The expressions for $W_{1,2}(\beta)$ are normalized under the no-overlap assumption made for α , which also implies that $C_{1,2}(\beta)$ integrate to 0.
 25. Barnett, S. M. & Radmore, P. M. *Methods in Theoretical Quantum Optics* (Clarendon Press, 2002).
 26. Grimm, A., Frattini, N. E., Puri, S., Mundhada, S. O., Touzard, S., Mirrahimi, M., Girvin, S. M., Shankar, S. & Devoret, M. H. Stabilization and operation of a Kerr-cat qubit. *Nature* **584**, 205–209. <https://www.nature.com/articles/s41586-020-2587-z> (2020).
 27. Lescanne, R., Villiers, M., Peronnin, T., Sarlette, A., Delbecq, M., Huard, B., Kontos, T., Mirrahimi, M. & Leghtas, Z. Exponential suppression of bit-flips in a qubit encoded in an oscillator. *Nature Physics* **16**, 509–513. <https://www.nature.com/articles/s41567-020-0824-x> (2020).
 28. Glauber, R. J. The Quantum Theory of Optical Coherence. *Physical Review* **130**, 2529–2539. <https://link.aps.org/doi/10.1103/PhysRev.130.2529> (1963).
 29. Miller, D. E., Anglin, J. R., Abo-Shaeer, J. R., Xu, K., Chin, J. K. & Ketterle, W. High-Contrast Interference in a Thermal Cloud of Atoms. *Physical Review A* **71**, 043615. <https://link.aps.org/doi/10.1103/PhysRevA.71.043615> (2005).
 30. Margalit, Y., Zhou, Z., Machluf, S., Japha, Y., Moukouri, S. & Folman, R. Analysis of a High-Stability Stern–Gerlach Spatial Fringe Interferometer. *New Journal of Physics* **21**, 073040. <https://iopscience.iop.org/article/10.1088/1367-2630/ab2fdc> (2019).
 31. Bloch, I., Hänsch, T. W. & Esslinger, T. Measurement of the Spatial Coherence of a Trapped Bose Gas at the Phase Transition. *Nature* **403**, 166–170. <https://www.nature.com/articles/35003132> (2000).
 32. Deléglise, S., Dotsenko, I., Sayrin, C., Bernu, J., Brune, M., Raimond, J.-M. & Haroche, S. Reconstruction of Non-Classical Cavity Field States with Snapshots of Their Decoherence. *Nature* **455**, 510–514. <https://www.nature.com/articles/nature07288> (2008).
 33. Kirchmair, G., Vlastakis, B., Leghtas, Z., Nigg, S. E., Paik, H., Ginossar, E., Mirrahimi, M., Frunzio, L., Girvin, S. M. & Schoelkopf, R. J. Observation of quantum state collapse and revival due to the single-photon Kerr effect. *Nature* **495**, 205–209. <https://www.nature.com/articles/nature11902> (2013).
 34. Milul, O., Guttel, B., Goldblatt, U., Hazanov, S., Joshi, L. M., Chausovsky, D., Kahn, N., Çiftçiyök, E., Lafont, F. & Rosenblum, S. Superconducting Cavity Qubit with Tens of Milliseconds Single-Photon Coherence Time. *PRX Quantum* **4**, 030336. <https://link.aps.org/doi/10.1103/PRXQuantum.4.030336> (2023).
 35. Samanta, C., De Bonis, S. L., Møller, C. B., Tormo-Queralt, R., Yang, W., Urgell, C., Stamenic, B., Thibeault, B., Jin, Y., Czaplowski, D. A., Pistolesi, F. & Bachtold, A. Nonlinear Nanomechanical Resonators Approaching the Quantum Ground State. *Nature Physics* **19**, 1340–1344. <https://www.nature.com/articles/s41567-023-02065-9> (2023).

36. Gutierrez Latorre, M., Higgins, G., Paradkar, A., Bauch, T. & Wieczorek, W. Superconducting Microsphere Magnetically Levitated in an Anharmonic Potential with Integrated Magnetic Readout. *Physical Review Applied* **19**, 054047. <https://link.aps.org/doi/10.1103/PhysRevApplied.19.054047> (2023).
37. Hofer, J., Gross, R., Higgins, G., Huebl, H., Kieler, O. F., Kleiner, R., Koelle, D., Schmidt, P., Slater, J. A., Trupke, M., Uhl, K., Weimann, T., Wieczorek, W. & Aspelmeyer, M. High-Q Magnetic Levitation and Control of Superconducting Microspheres at Millikelvin Temperatures. *Physical Review Letters* **131**, 043603. <https://link.aps.org/doi/10.1103/PhysRevLett.131.043603> (2023).
38. Millen, J., Fonseca, P. Z. G., Mavrogordatos, T., Monteiro, T. S. & Barker, P. F. Cavity Cooling a Single Charged Levitated Nanosphere. *Physical Review Letters* **114**, 123602. <https://link.aps.org/doi/10.1103/PhysRevLett.114.123602> (2015).
39. Delord, T., Huillery, P., Nicolas, L. & Hétet, G. Spin-Cooling of the Motion of a Trapped Diamond. *Nature* **580**, 56–59. <https://www.nature.com/articles/s41586-020-2133-z> (2020).
40. Conangla, G. P., Rica, R. A. & Quidant, R. Extending Vacuum Trapping to Absorbing Objects with Hybrid Paul-Optical Traps. *Nano Letters* **20**, 6018–6023. <https://doi.org/10.1021/acs.nanolett.0c02025> (2020).
41. Dania, L., Bykov, D. S., Goschin, F., Teller, M., Kassid, A. & Northup, T. E. Ultrahigh Quality Factor of a Levitated Nanomechanical Oscillator. *Physical Review Letters* **132**, 133602. <https://link.aps.org/doi/10.1103/PhysRevLett.132.133602> (2024).
42. Horowitz, P. & Hill, W. *The art of electronics* 2nd ed (Cambridge University Press, 1989).
43. Diedrich, F., Bergquist, J. C., Itano, W. M. & Wineland, D. J. Laser Cooling to the Zero-Point Energy of Motion. *Physical Review Letters* **62**, 403–406. <https://link.aps.org/doi/10.1103/PhysRevLett.62.403> (1989).
44. Hamann, S. E., Haycock, D. L., Klose, G., Pax, P. H., Deutsch, I. H. & Jessen, P. S. Resolved-Sideband Raman Cooling to the Ground State of an Optical Lattice. *Physical Review Letters* **80**, 4149–4152. <https://link.aps.org/doi/10.1103/PhysRevLett.80.4149> (1998).
45. Johansson, J. R., Nation, P. D. & Nori, F. QuTiP 2: A Python Framework for the Dynamics of Open Quantum Systems. *Computer Physics Communications* **184**, 1234–1240. <https://www.sciencedirect.com/science/article/pii/S0010465512003955> (2013).

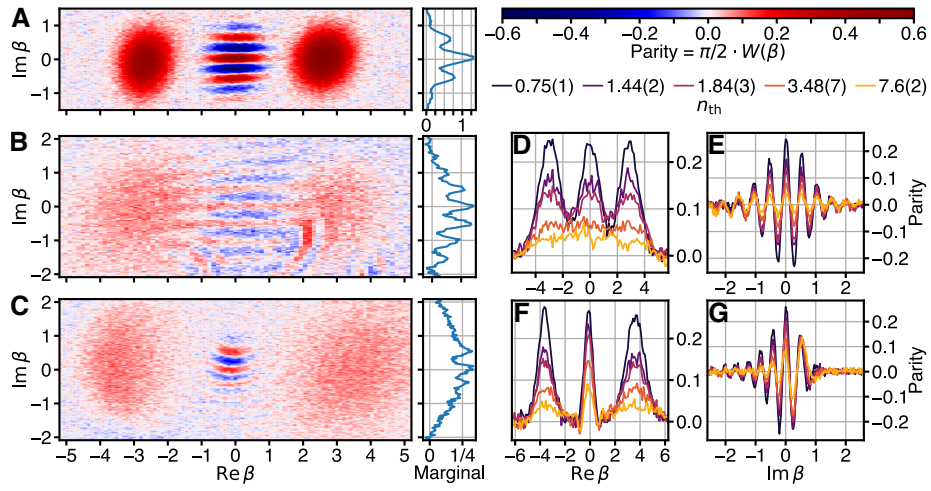


Fig. 1. Wigner function measurement results. (A) Cold Schrödinger cat prepared using the qcMAP protocol with the heat bath disconnected ($n_{\text{th}} = 0.03$, $\mathcal{P} = 0.94$). (B,C) ‘Hot’ Schrödinger cat states prepared from an initial thermal state with $n_{\text{th}} = 3.48(7)$ using the ECD (B) and qcMAP (C) protocols. Also displayed in A-C are the marginal distributions obtained by summation along the $\text{Re}\{\beta\}$ axis. To increase the visibility of small parity values, the color brightness changes nonlinearly across the colorbar. (D-G) Linecuts of the Wigner function along the coordinate axes in the ECD (D,E) and qcMAP (F,G) protocols with n_{th} of the initial state as indicated in the legend.

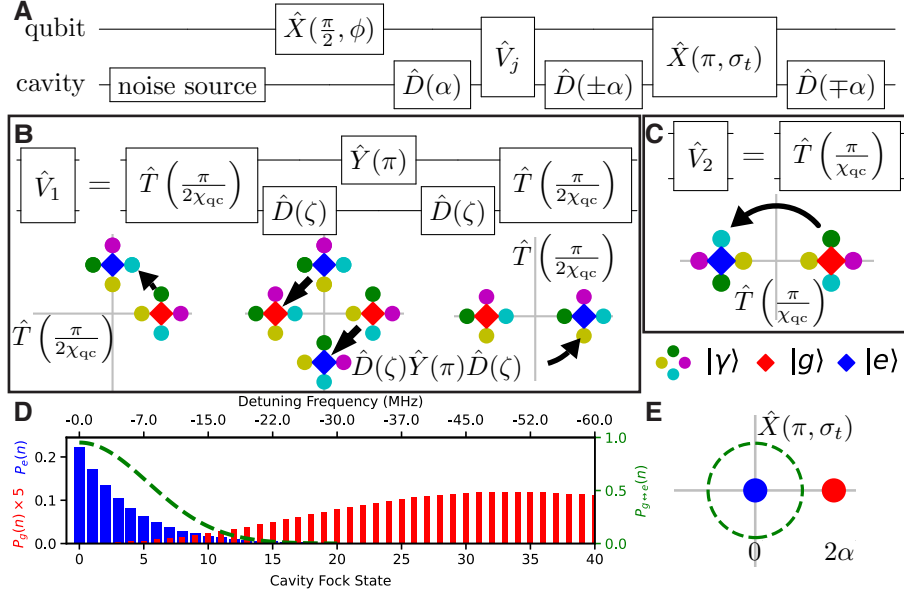


Fig. 2. Hot cat state generation protocol. (A) Quantum circuit diagram of hot cat state generation sequence. For ECD (qcMAP), $j = 1$ ($j = 2$), and the displacements use the lower (upper) sign. $\hat{X}(\pi/2, \phi)$ is a qubit $\pi/2$ pulse with phase ϕ , and $\hat{X}(\pi, \sigma_t)$ is the disentanglement pulse. (B) Definition of \hat{V}_1 and visualization of its action in the joint cavity-qubit phase space. $\hat{T}(t)$ denotes free evolution for time t , $\hat{Y}(\pi)$ is a qubit π pulse, and $\zeta = -(1+i)\alpha/2$. Cavity states are entangled with the qubit states whose marker they touch. The arrows illustrate how the total state evolves under the indicated operator. (C) Definition and visualization of \hat{V}_2 . (D) Qubit-conditional cavity Fock state distributions $P_q(n) = \langle n | \langle q | \hat{\rho} | q \rangle | n \rangle$, ($q \in \{g, e\}$) of the total state before the $\hat{X}(\pi, \sigma_t)$ operation. Here $\alpha = 3$ and $n_{th} = 3.5$. The dashed line shows $P_{g \leftrightarrow e}(n)$ (defined in the main text) with $\sigma_t = 20$ ns. (E) The choice of σ_t corresponds to the choice of a radius in the cavity-qubit phase space within which the qubit state is flipped with a certain probability. At this stage of the protocol, the $|g\rangle$ branch is displaced by 2α .

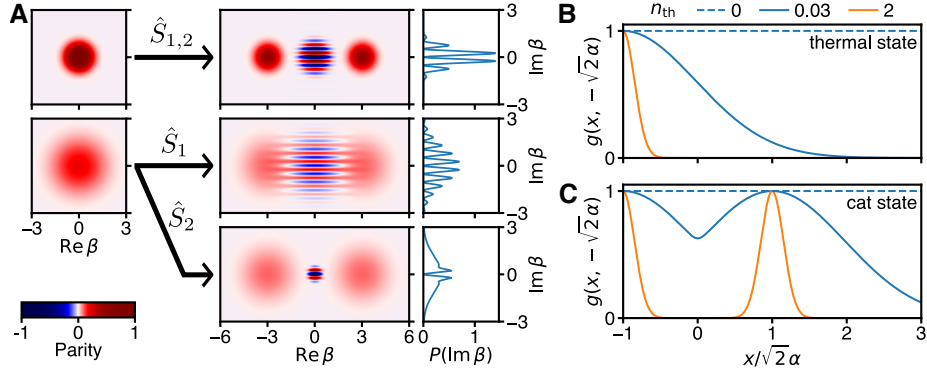


Fig. 3. Hot Schrödinger Cat States in Theory. (A) Left: Plots of the thermal state Wigner function $W_T(\beta)$ with $n_{\text{th}} = 0$ (top), $n_{\text{th}} = 2$ (middle). To increase the visibility of the hotter state, the color brightness changes nonlinearly across the colorbar (bottom). Center: Cat state Wigner functions $W_{1,2}(\beta)$ which result from applying the operators $\hat{S}_{1,2}$ with $\alpha = 3.5$ and $\phi = \pi$ to the initial states on the left according to the arrows. Right: Marginal probability distributions obtained from the cat state Wigner functions by integrating along the $\text{Re}\{\beta\}$ axis. (B) Sections of the coherence function $g(x_1, x_2)$ for the thermal states. The number in the legend indicates the n_{th} of the state. (C) Sections of the coherence function $g(x_1, x_2)$ for the cat states (lower panel) along the line from $(x_1, x_2) = \sqrt{2}\alpha(-1, -1)$ to $(x_1, x_2) = \sqrt{2}\alpha(3, -1)$. The plots are made with $\alpha = 3.5$.

Supplemental Material for Hot Schrödinger Cat States

Ian Yang^{1,2}, Thomas Agrenius^{2,3}, Vasilisa Usova^{1,2}, Oriol Romero-Isart^{2,3,*},
Gerhard Kirchmair^{1,2,**}

¹Institute for Experimental Physics, University of Innsbruck, 6020 Innsbruck, Austria

²Institute for Quantum Optics and Quantum Information, Austrian Academy of Sciences, 6020 Innsbruck, Austria

³Institute for Theoretical Physics, University of Innsbruck, 6020 Innsbruck, Austria

*Present address: ICFO - Institut de Ciències Fotoniques, The Barcelona Institute of Science and Technology, Castelldefels (Barcelona) 08860, Spain and ICREA, Passeig Lluís Companys 23, 08010, Barcelona, Spain

**To whom correspondence should be addressed; E-mail: gerhard.kirchmair@uibk.ac.at

Contents

S1 Experiment	12
S1.1 Experimental Setup	12
S1.2 Calibration and Scaling of Wigner Function	15
S1.3 Additional Hot Cat Wigner Function Measurements	17
S1.4 Characterizing the Initial Thermal State	19
S1.5 Characterization of Hamiltonian	21
S2 Theory	24
S2.1 Theoretical analysis of the qcMAP and ECD protocols	24
S2.2 Derivation of the Wigner functions $W_{1,2}(\beta)$ from the operators $\hat{S}_{1,2}$	28
S2.3 Hot cat state coherence functions	29
S3 Numerical model	33
S3.1 Method	33
S3.2 Comparison of Simulation and Data	34
S4 Analysis of Imperfections	37
S4.1 Residual cavity-qubit entanglement	37
S4.2 Comparison of simulations with different parameters	37
S4.3 Free evolution timing errors	40

S1 Experiment

S1.1 Experimental Setup

The schematic of the experimental setup is shown in Figure S1. The high coherence cavity has a post length of 14.8 mm, inner radius of 2 mm and outer radius of 6.4 mm. This geometry gives a bare cavity frequency of approximately 4.5 GHz. The tunnel for the qubit chip has a diameter of 4 mm, which is a compromise between cavity mode leakage into the tunnel and qubit capacitance to ground. The cavity was made from high-purity niobium at the Institute for Quantum Optics and Quantum Information Innsbruck mechanical workshop. The manufacturing process used electro-discharge machining with a tungsten alloy electrode. The cavity was then etched with our collaborators at the Institute of Science and Technology, Vienna with the group of Prof. Johannes Fink. This process used a buffer chemical polishing etching solution of 1:1:1 hydrofluoric, nitric and phosphoric acid for one hour at 5 °C. Phosphoric acid was then slowly added to reach a ratio of 1:1:2 for another hour of polishing. Afterwards, the niobium cavity was rinsed heavily with deionized (DI) water. In total, this process removes approximately 150 μm of material.

The transmon qubit and readout resonator were patterned by electron-beam lithography (Raith eLINE Pllus 30 kV) on a bi-layer resist (1 μm MMA (8.5) EL13 and 0.3 μm of 950 PMMA A4). The substrate started from a 2-inch sapphire wafer that was first piranha-cleaned before processing. To prevent charging of the substrate, a thin gold layer was sputtered on top of the PMMA. After lithography, this gold layer was etched in a solution of Lugol (5 % potassium iodide) and DI water in a ratio of 1:15, before being washed in DI water and developed in a 3:1 solution of isopropyl alcohol and water. In the next step, two layers of aluminum (25 nm and 50 nm) were evaporated onto the sample using a Plassys MEB550S electron-beam evaporator. A controlled oxidation step (5 mbar for 5.5 min) was carried out in between the deposition of the two aluminum layers. Subsequently, the qubit chip was laser-diced, and the resist layer was lifted off. The sample chips were thermalized by a copper clamp. An additional aluminum sheet was used to cover the copper clamp to reduce losses due to the presence of the copper material.

The measurements were conducted in a Triton DU7-200 Cryofree dilution refrigerator system. The input coaxial cables were attenuated by 20 dB at the 4 K plate and 10 dB at the still plate. Finally, at the mixing chamber plate, the input signal was filtered by a K&L DC-12 GHz low pass filter and then attenuated by a 20 dB directional coupler followed by a thermalized cryogenic 20 dB attenuator and filtered by microtronics 4 – 8 GHz bandpass filter. The experiment was done in reflection with a Quinstar double junction 4 – 8 GHz circulator. Before and after the sample, the input and output signals passed through a home-built eccosorb filter. The input signal for the high coherence cavity was attenuated and filtered similarly, except at the base plate where a 10 dB thermalized cryogenic attenuator was used instead.

The output signal was filtered via a microtronics 4 – 8 GHz bandpass filter, before passing through a quantum-limited parametric amplifier. Finally, the output signal was filtered by a K&L filter which was connected to two Quinstar isolators giving 40 dB isolation. The signal was amplified at the 4 K plate by high electron mobility transistor (HEMT) amplifiers and again with room temperature amplifiers outside of the refrigerator.

Control of the thermal noise was done by amplifying and filtering the noise from a 50 Ω resistor. The added noise has a frequency spectrum shown in Figure S3A. The added noise power level was controlled by a digital attenuator. A fast, home-built microwave switch was used to disconnect the cavity mode from this added noise. To initialize the cavity state, the cavity mode was allowed to come into thermal equilibrium with the controlled noise environment for 1 ms. Afterwards, the microwave switch was opened and the state preparation and measurement started.

Leaving the microwave switch opened resulted in a thermal state in equilibrium with the residual thermal excitations of the setup ($n_{\text{th}} = 0.0338(7)$), which was the coldest initial state we could achieve with this setup.

The samples were placed in a μ -metal shield which sat in a superconducting shield to protect the experiment against stray magnetic fields. The shield was filled with eccosorb foam for the absorption of any stray infrared photons.

The pulses for the high coherence cavity and readout resonator were generated by an arbitrary waveform generator (AWG), specifically the Operator X from Quantum Machines. These pulses were up-mixed with a local

oscillator (LO) using a Marki microwave IQ mixer. The qubit pulses, on the other hand, were up-mixed through a double-super-heterodyne [42] setup employing two LOs and two single side-band mixers. These pulse generation setups also incorporated various amplifiers, filters, alternators, and fast microwave switches to achieve effective suppression of unwanted mixing products and to minimize leakage of LO signals. The signal from the refrigerator was down-mixed using the same readout LO and further amplified before being digitized by Operator X from Quantum Machines.

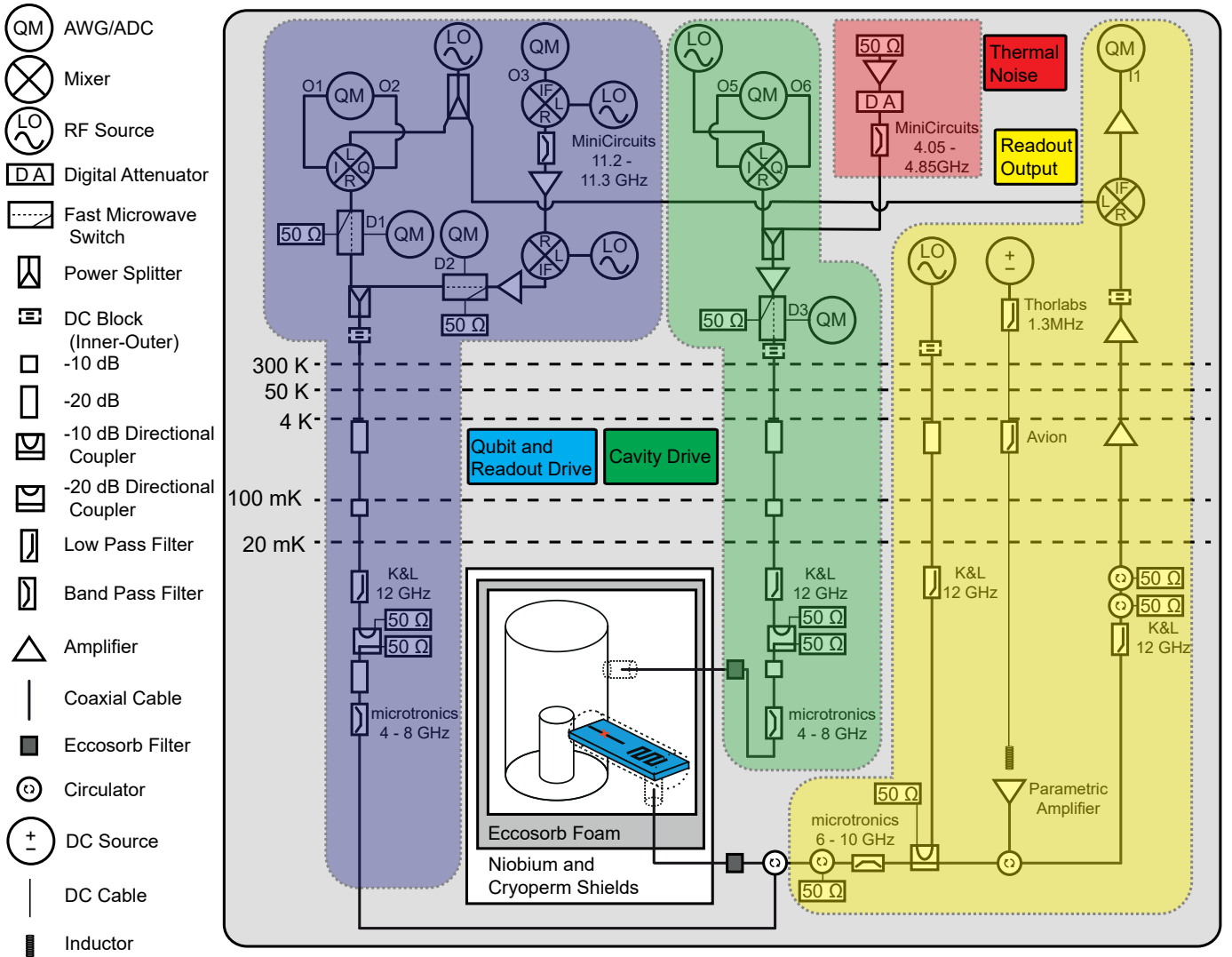


Fig. S1. Schematic of Experimental Wiring. The cavity and readout resonator were driven by an IQ mixing setup while the qubit tones were up-converted via a double-super-heterodyne setup. The qubit-resonator line had a total of 70 dB input line attenuation while the cavity had 60 dB. Cavity noise was added via amplifying Johnson-Nyquist noise at room temperature and filtered with a MiniCircuits filter. The noise level was reduced by a digital attenuator. The readout tone was first amplified with a parametric amplifier before reaching the HEMTs. Noise from the output and amplifier pump lines were attenuated with isolators. Additional microwave and eccosorb filters were used to remove unwanted radiation from reaching the experiment. The setup was placed in superconducting and μ -metal shields and was surrounded by eccosorb foam.

S1.2 Calibration and Scaling of Wigner Function

The Wigner function measurement was calibrated by the measurement of a single photon Fock state. The single photon Fock state was prepared by using a blue sideband transition. This technique is similar to that used in ion traps [43] or atomic arrays [44]. The measurement data, which has arbitrary units, was collected in the pulse quadrature variables I, Q , which also have arbitrary units (Figure S2A). To calibrate the measurement, we seek a linear map from the data space into phase space. We find this map by fitting the function $\chi_W^{-1} W_{|1\rangle}(\chi_I I + i\chi_Q Q)$ to the Fock state measurement data, where χ_W, χ_I , and χ_Q are scaling constants, and $W_{|1\rangle}(\beta)$ is the Wigner function of the first Fock state (Figure S2B,C). Using the fitted scaling constants, we then map all other Wigner function measurement data into phase-space by constructing $\beta = \chi_I I + i\chi_Q Q$ and $W(\beta) = \chi_W D(I, Q)$, where $D(I, Q)$ is the measurement data.

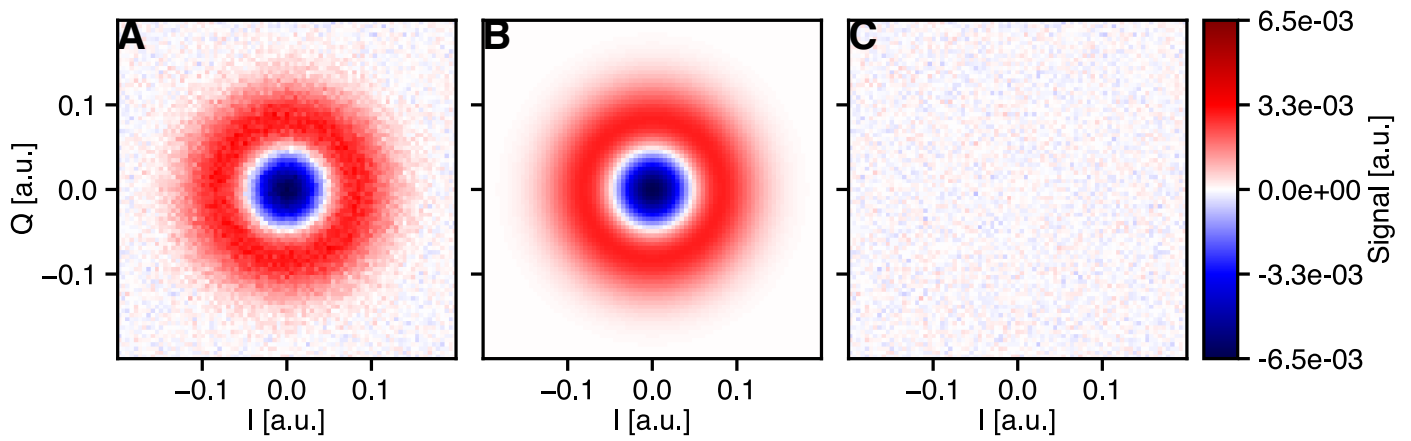


Fig. S2. Wigner Measurement and Fit of a Single Photon Fock State. (A) Measured data and (B) analytical fit of a $|1\rangle$ cavity Fock state in data space. (C) Residuals of fit. We use the parameters of the fit to construct a linear map from data space into phase space (Section S1.2).

S1.3 Additional Hot Cat Wigner Function Measurements

In Figure S3, we report Wigner function measurements on states prepared by the qcMAP and ECD protocols in an earlier experimental setup. In this setup, we had $\chi_{qc}/2\pi = 1.272$ MHz, $K_c/2\pi = 2.33$ kHz, $\chi'_{qc}/2\pi = 7.1$ kHz, cavity lifetime $T_{1,c} = 128$ μ s, qubit lifetime $T_1 = 6.3$ μ s, and qubit coherence time $T_2^* = 2.4$ μ s. In these experimental runs, the heat bath used to prepare the initial state was kept connected throughout the preparation and measurement protocol. Note that, in our setup, the cavity lifetime is limited by the external coupling via the coupling pin to the environment. Thus, the cavity coupling rate to the heat bath is the same as the cavity photon loss rate. The experiment was run with $\alpha = 2.5$ and $n_{th} = 2.07$.

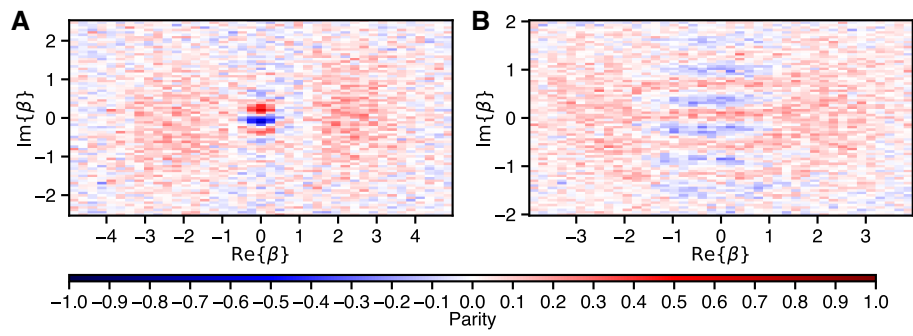


Fig. S3. Hot cat state measurements from a previous experimental setup with the heat bath left connected. (A) qcMAP protocol (B) ECD protocol. Note that this plot uses a linear scaling of the color bar. See section S1.3 for the parameters of this setup.

S1.4 Characterizing the Initial Thermal State

To determine the initial thermal state of the cavity mode, number-split qubit spectroscopy was performed (Figure S4). This allowed for the measurement of the cavity photon distribution. The steps involved are shown in Figure S4B. First, the cavity mode was equilibrated with the thermal bath as described in Section S1.1. Next, a cavity photon number selective qubit π -pulse was applied and the qubit state was measured. By repeating the measurement to get an ensemble average, the probability to excite the qubit at a certain frequency was determined.

Due to the cavity photon distribution and the dispersive coupling between the cavity and the qubit, the qubit resonance frequency is split into a spectrum of multiple frequencies where the relative resonance peak height depends on the cavity photon distribution (Figure S4C). By measuring the probability to excite the qubit across the frequency spectrum, we also directly measure the cavity photon number distribution.

For a thermal state with average photon occupation number n_{th} , the probability of measuring n photons is

$$P_{n_{\text{th}}}(n) = \frac{n_{\text{th}}^n}{(1 + n_{\text{th}})^{n+1}}. \quad (\text{S1})$$

By fitting this to the spectral qubit excitation probability (Figure S4C), we determined n_{th} of the cavity state. By varying the added photon noise power, we found a relationship between the attenuator setting and n_{th} (Figure S4D).

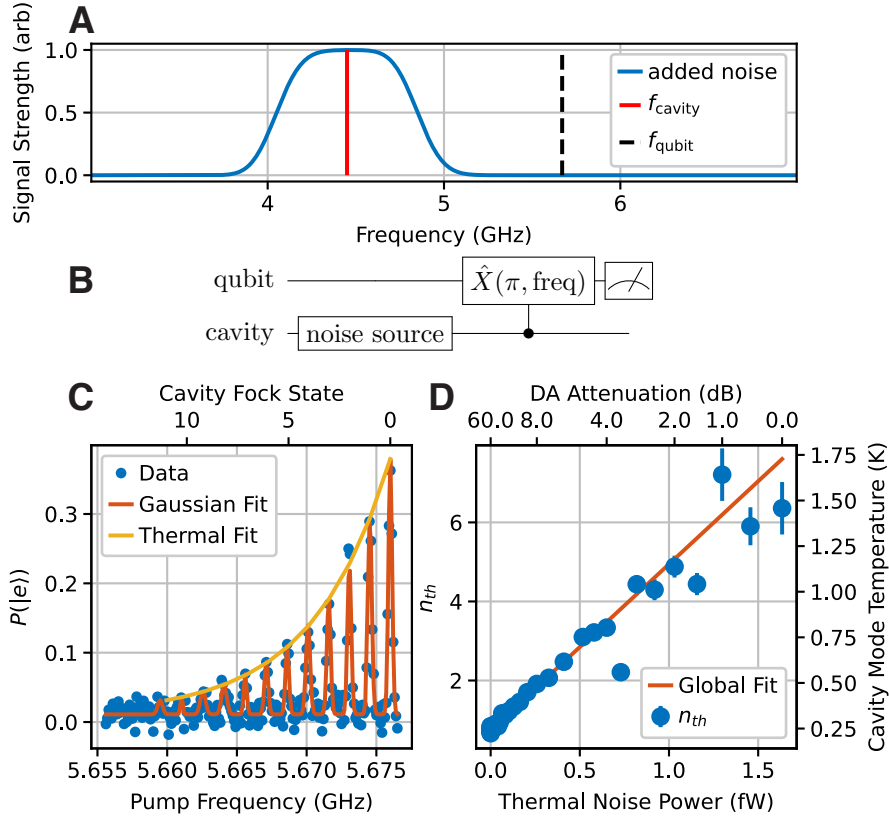


Fig. S4. Thermal State Measurement Technique (A) An illustration of frequency spectrum of the added noise. The thermal noise is only added at the cavity frequency while qubit frequencies are filtered out. The noise level is controlled by a digital attenuator. (B) Experimental Pulse sequence. (C) Qubit spectroscopy measurement result for a thermal state. Here, $n_{\text{th}} = 3.3(1)$. (D) Thermal population measurements for different attenuation settings, corresponding to noise powers. The added noise power with the mean thermal photon is fitted with a straight line.

S1.5 Characterization of Hamiltonian

The full system Hamiltonian, including perturbative terms due to higher excitation levels of the qubit and cavity nonlinearities, is

$$\hat{H}/\hbar = \omega_c \hat{c}^\dagger \hat{c} - \frac{K_c}{2} \hat{c}^\dagger \hat{c}^\dagger \hat{c} \hat{c} + \omega_q \hat{q}^\dagger \hat{q} - \frac{K_q}{2} \hat{q}^\dagger \hat{q}^\dagger \hat{q} \hat{q} - \chi_{qc} \hat{c}^\dagger \hat{c} \hat{q}^\dagger \hat{q} - \frac{K'_c}{6} \hat{c}^\dagger \hat{c}^\dagger \hat{c}^\dagger \hat{c} \hat{c} \hat{c} - \frac{\chi'_{qc}}{2} \hat{c}^\dagger \hat{c}^\dagger \hat{c} \hat{c} \hat{q}^\dagger \hat{q} \quad (\text{S2})$$

Here \hat{q}^\dagger and \hat{c}^\dagger are the creation operators for the qubit and cavity mode respectively, and \hat{q} , \hat{c} are the corresponding annihilation operators. The values of the Hamiltonian parameters were measured experimentally and are reported in Table S1.

To characterize the Hamiltonian of our system, we employed a measurement method to accurately determine the cavity frequency as a function of the cavity photon number and qubit initial state (Figure S6A). A similar technique was reported in [11]. First, the cavity was displaced by β and allowed to evolve for a time delay t , with the qubit in the ground state. The delay time was varied up to a maximum delay time, T . Subsequently, a second displacement with displacement parameter $\beta \exp\{-i\phi(t)\}$ was applied, where $\phi(t) = 2\pi \times 5t/T$. Finally, a cavity ground state selective π -pulse (described by the operator $\hat{X}(\pi, \sigma_t)$ with $\sigma_t = 300$ ns) was applied to the qubit, and the qubit state was measured.

The principle of the measurement is illustrated in Figure S6B. For weak Kerr effects and the qubit in the ground state, the displaced state approximately evolves as $|\beta e^{i\omega(\beta)t}\rangle$, where

$$\omega(\beta) = \Delta - |\beta|^2 \frac{K_c}{2} - |\beta|^4 \frac{K'_c}{6}, \quad (\text{S3})$$

and the cavity frequency detuning $\Delta = \omega_c - \omega_{\text{drive}}$ from the drive frequency ω_{drive} . The ground-state selective π -pulse will flip the qubit only if $\phi(t)$ in the second displacement pulse matches $\omega(\beta)$, i.e. $\phi(t) = \omega(\beta)$. Thus, the probability of measuring the cavity in the ground state, or equivalently, qubit in the excited state, is expected to be

$$P(|e\rangle) = |\langle 0|\beta(t)\rangle|^2 = e^{-2|\beta|^2[1 - \cos(\omega(\beta)t)] - t/T_{1,c}}, \quad (\text{S4})$$

The exponential decay comes from the finite cavity lifetime.

We measure $P(|e\rangle)$ as a function of t and β (Figure S6C). We then fit Eq. (S4) as a function of t for the different values of β used in the measurement (Figure S6D). From the fit, we extract $\omega(\beta)$ for the given value of β . We then fit Eq. (S3) to the measured $\omega(\beta)$ to extract Δ , K_c , and K'_c (Figure S6E). Finally, we repeat the procedure with the qubit initially in the excited state, which allows us to determine χ_{qc} and χ'_{qc} .

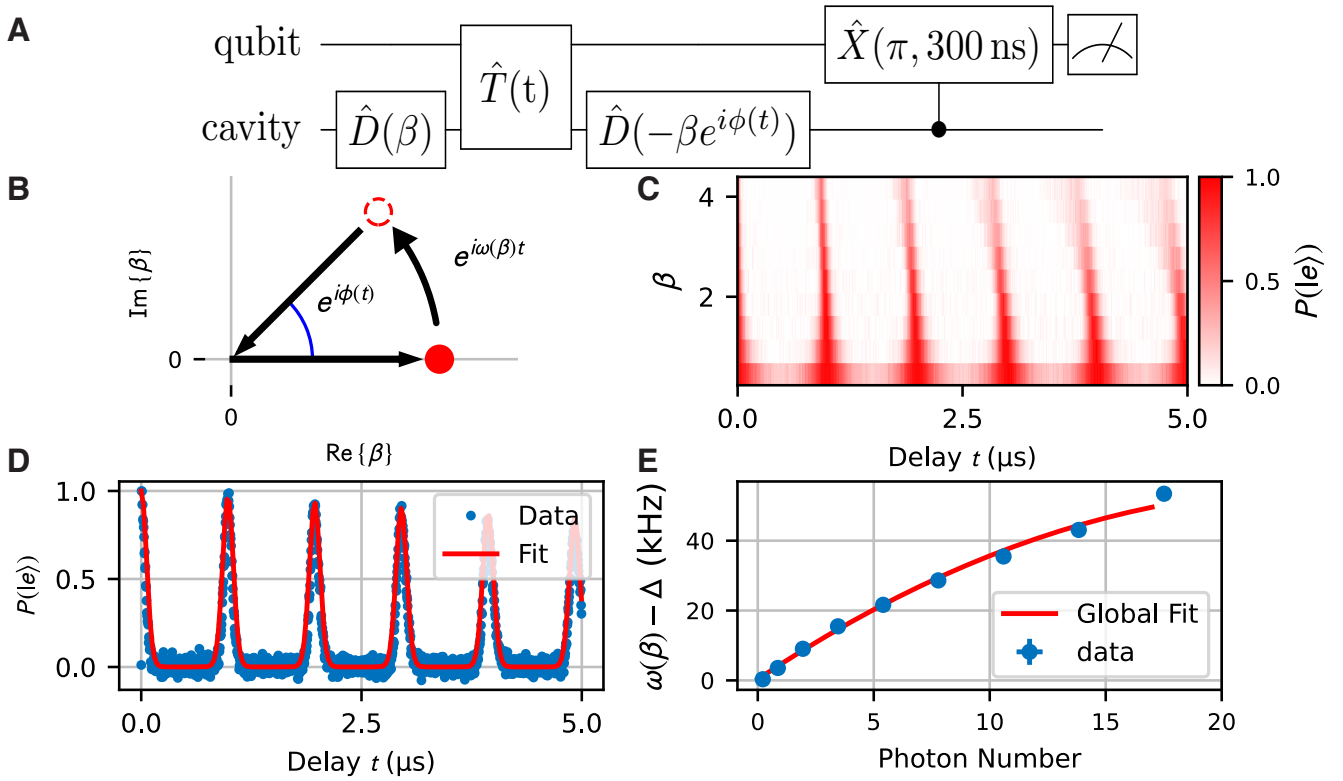


Fig. S6. Hamiltonian Measurement Technique (A) Experimental pulse sequence. (B) Phase space evolution of the cavity during the experiment. (C) Measurement data of the qubit excited state probability for different values of the delay time and the initial displacement. Here, the qubit is initialized in the ground state. (D) Measurement of the qubit excited state probability for a fixed value of β . The solid line is a fit of Eq. (S4). (E) The photon-number dependent cavity frequency $\omega(\beta)$ as a function of the initial average photon number $|\beta|^2$ with a fit of Eq. (S3).

Parameter	Symbol	Value
Qubit Frequency	$\omega_q/2\pi$	5.676001 GHz
Qubit Anharmonicity	$K_q/2\pi$	189.9 ± 0.4 MHz
Qubit Lifetime	T_1	31.0 ± 0.4 μ s
Qubit Coherence Time	T_2^*	12.5 ± 0.4 μ s
Qubit Hann Echo Time	T_2^E	16.9 ± 0.5 μ s
High Q Cavity Frequency	$\omega_c/2\pi$	4.544939 GHz
High Q Cavity Self-Kerr	$K_c/2\pi$	4.9 ± 0.1 kHz
High Q Cavity Second Order Self-Kerr	$K'_c/2\pi$	14 ± 8 Hz
High Q Cavity Lifetime	$T_{1,c}$	110 ± 2 μ s
High Q Cavity - Qubit Dispersive Shift	$\chi_{qc}/2\pi$	1.499 ± 0.003 MHz
High Q Cavity - Qubit Second Order Dispersive shift	$\chi'_{qc}/2\pi$	12.8 ± 0.9 kHz
High Q Cavity Residual Mean Thermal Photon Number	$n_{th, residual}$	0.0338 ± 0.007
High Q Cavity Residual Mode Temperature	$T_{cavity, residual}$	63.7 ± 0.4 mK
Qubit Residual Mode Temperature	T_{qubit}	68 ± 1 mK
Readout Resonator Frequency	$\omega_r/2\pi$	7.528852 GHz
Readout Resonator External Coupling	$\kappa_{c ext}/2\pi$	1.33 MHz
Readout Resonator - Qubit Dispersive Shift	$\chi_{rq}/2\pi$	1.61 MHz
Readout Resonator - High Q Cavity Dispersive Shift (calculated)	$\chi_{rc,cal}/2\pi$	3.4 kHz

Table. S1. Hamiltonian Parameters. The high Q cavity lifetime is limited by its external coupling. The reported cross Kerr $\chi_{readout-cavity,cal}$ is a lower bound calculated via $\chi_{rc} = \chi_{qc}\chi_{qr}(\frac{1}{\Delta_{qc}} + \frac{1}{\Delta_{qr}})$.

S2 Theory

We show that the qcMAP and ECD protocols are described by the operators $\hat{S}_{1,2}$ under ideal conditions, derive the hot cat Wigner functions $W_{1,2}(\beta)$, and analyze the coherence functions of the hot cats.

S2.1 Theoretical analysis of the qcMAP and ECD protocols

In this section, we show that the ECD and qcMAP pulse sequences displayed in the quantum circuit diagrams in Figure 2A-C are respectively equivalent to applying the operators \hat{S}'_1 and \hat{S}'_2 to the initial cavity state $\hat{\rho}_0$. A necessary condition is that $\hat{\rho}_0$ has no overlap with itself when displaced by 2α . We repeat the operator definitions from the main text for convenience. The equivalent operator for the ECD protocol is

$$\hat{S}'_1 \equiv \frac{1}{\sqrt{2}} \left[\hat{D}(\alpha) - e^{i(\phi+2|\alpha|^2)} \hat{D}(-\alpha) \right] i^{\hat{n}}, \quad (\text{S5})$$

which in turn is equivalent to the operator

$$\hat{S}_1 \equiv \frac{1}{\sqrt{2}} \left[\hat{D}(\alpha) + e^{i\phi} \hat{D}(-\alpha) \right] \quad (\text{S6})$$

when the initial state is thermal and ϕ is experimentally controllable. The equivalent operator for the qcMAP protocol is

$$\hat{S}_2 \equiv \frac{1}{\sqrt{2}} \left[1 - e^{i\phi} \hat{H} \right] \hat{D}(\alpha). \quad (\text{S7})$$

From Figure 2A-C, we read that the ECD and qcMAP protocols first prepare the initial thermal state $\hat{\rho}_0$ of the cavity and then apply the unitary operators

$$\hat{U}_1 \equiv \hat{D}(\alpha) \hat{X}(\pi, \sigma_t) \hat{D}(-\alpha) \hat{T}(\pi/2\chi_{\text{qc}}) \hat{D}[-\alpha \frac{(1+i)}{2}] \hat{Y}(\pi) \hat{D}[-\alpha \frac{(1+i)}{2}] \hat{T}(\pi/2\chi_{\text{qc}}) \hat{D}(\alpha) \hat{X}(\pi/2, \phi) \quad (\text{S8})$$

for ECD, and

$$\hat{U}_2 \equiv \hat{D}(-\alpha) \hat{X}(\pi, \sigma_t) \hat{D}(\alpha) \hat{T}(\pi/\chi_{\text{qc}}) \hat{D}(\alpha) \hat{X}(\pi/2, \phi) \quad (\text{S9})$$

for qcMAP, to the cavity-qubit initial state $\hat{\rho}_0|g\rangle\langle g|$ (we define all operators appearing in these expressions in the next paragraph). Under ideal conditions, the final state of the protocols is

$$\hat{U}_i \hat{\rho}_0 |g\rangle\langle g| \hat{U}_i^\dagger = \hat{\rho}_i |g\rangle\langle g| \quad (\text{S10})$$

($i \in \{1, 2\}$), with

$$\hat{\rho}_i \equiv \hat{S}_{gg,i} \hat{\rho}_0 \hat{S}_{gg,i}^\dagger, \quad (\text{S11})$$

$$\hat{S}_{gg,i} \equiv \langle g | \hat{U}_i | g \rangle. \quad (\text{S12})$$

It is straightforward to show that the final cavity-qubit state Eq. (S10) is a product state, with the qubit in the $|g\rangle$ state, if and only if

$$\text{Tr} \{ \hat{S}_{gg,i} \hat{\rho}_0 \hat{S}_{gg,i}^\dagger \} = 1. \quad (\text{S13})$$

Consequently, the ECD and qcMAP protocols, given exactly by $\hat{U}_{1,2}$, are equivalent to the operators $\hat{S}_{gg,\{1,2\}}$ for all initial states $\hat{\rho}_0$ which satisfy Eq. (S13).

The operators appearing in Eqs. (S8) and (S9) are: I) The cavity displacement operator

$$\hat{D}(\beta) \equiv \exp \{ \beta \hat{c}^\dagger - \beta^* \hat{c} \} \quad (\text{S14})$$

where \hat{c}, \hat{c}^\dagger are the cavity annihilation and creation operators and β is a complex-valued argument. II) The time-evolution operator under the dispersive interaction Hamiltonian $\hat{T}(t)$. The interaction Hamiltonian is $\hat{H} = -\hbar\chi_{\text{qc}}\hat{n}|e\rangle\langle e|$, where $\hat{n} = \hat{c}^\dagger\hat{c}$, so the time-evolution operator is

$$\hat{T}(t) = \exp\{it\chi_{\text{qc}}\hat{n}|e\rangle\langle e|\} = |g\rangle\langle g| + \exp\{it\chi_{\text{qc}}\hat{n}\}|e\rangle\langle e|. \quad (\text{S15})$$

In particular,

$$\hat{T}(\pi/\chi_{\text{qc}}) = |g\rangle\langle g| + \hat{H}|e\rangle\langle e| \quad (\text{S16})$$

where $\hat{H} = (-1)^{\hat{n}}$ is the parity operator, and

$$\hat{T}(\pi/2\chi_{\text{qc}}) = |g\rangle\langle g| + i^{\hat{n}}|e\rangle\langle e|. \quad (\text{S17})$$

In phase space, the operator $i^{\hat{n}}$ leads to a counterclockwise rotation by $\pi/2$ around the phase-space origin. III) The qubit rotation operators acting only on the qubit Hilbert space

$$\hat{X}(\pi/2, \phi) \equiv \frac{1}{\sqrt{2}} [(|g\rangle + ie^{i\phi}|e\rangle)\langle g| + (|e\rangle + ie^{-i\phi}|g\rangle)\langle e|], \quad (\text{S18})$$

where ϕ is an experimentally controllable phase,

$$\hat{X}(\pi) \equiv i(|g\rangle\langle e| + |e\rangle\langle g|), \quad (\text{S19})$$

and

$$\hat{Y}(\pi) \equiv \hat{R}(\pi, \pi/2) = |g\rangle\langle e| - |e\rangle\langle g|. \quad (\text{S20})$$

These operators are special cases of the general qubit rotation operator

$$\hat{R}(a, \mathbf{u}) \equiv \exp\left\{\frac{ia}{2}\mathbf{u} \cdot \hat{\boldsymbol{\sigma}}\right\} = \hat{1} \cos \frac{a}{2} + i\mathbf{u} \cdot \hat{\boldsymbol{\sigma}} \sin \frac{a}{2} \quad (\text{S21})$$

with a a real variable, \mathbf{u} a unit vector on the 3-dimensional unit sphere, and $\hat{\boldsymbol{\sigma}} = \hat{\sigma}_x\mathbf{e}_x + \hat{\sigma}_y\mathbf{e}_y + \hat{\sigma}_z\mathbf{e}_z$ (\mathbf{e}_j are the coordinate unit vectors and $\hat{\sigma}_j$ the Pauli matrices $\hat{\sigma}_x = |g\rangle\langle e| + |e\rangle\langle g|$, $\hat{\sigma}_y = i(-|g\rangle\langle e| + |e\rangle\langle g|)$, $\hat{\sigma}_z = |g\rangle\langle g| - |e\rangle\langle e|$). We have $\hat{X}(\pi/2, \phi) = \hat{R}(\pi/2, \cos\phi\mathbf{e}_x + \sin\phi\mathbf{e}_y)$, $\hat{X}(\pi) = \hat{R}(\pi, \mathbf{e}_x)$, $\hat{Y}(\pi) = \hat{R}(\pi, \mathbf{e}_y)$. IV) The cavity-selective qubit rotation operator $\hat{X}(\pi, \sigma_t)$. We assume that it takes the form

$$\hat{X}(\pi, \sigma_t) = \sum_{n=0}^{\infty} |n\rangle\langle n| \hat{R}(a_n, \mathbf{u}_n), \quad (\text{S22})$$

i.e. that it is defined by specifying a sequence of qubit rotation operators on the Fock states $|n\rangle$. We further assume that the parameters $\{a_n\}_{n=0}^{\infty}$ and $\{\mathbf{u}_n\}_{n=0}^{\infty}$ are such that for $n \leq N$, where N is a number that depends on σ_t , $a_n = \pi$ and $\mathbf{u}_n = \mathbf{e}_x$. Additionally, the sequence of parameters $\{a_n\}_{n=0}^{\infty}$ decays so that there is a number M (also determined by σ_t) such that $a_n = 0$ when $n > M$. In this case, we can write

$$\hat{X}(\pi, \sigma_t) = i\hat{P}_{\leq N}\hat{\sigma}_x + \hat{P}_{>M} + \hat{Q}_{NM}, \quad (\text{S23})$$

where we have introduced the operators

$$\hat{P}_{\leq N} \equiv \sum_{n=0}^N |n\rangle\langle n|, \quad (\text{S24})$$

$$\hat{P}_{>M} \equiv \sum_{n=M+1}^{\infty} |n\rangle\langle n|, \quad (\text{S25})$$

$$\hat{Q}_{NM} \equiv \sum_{n=N+1}^M |n\rangle\langle n| \hat{R}(a_n, \mathbf{u}_n). \quad (\text{S26})$$

It is possible (by using a Magnus approximation [20]) to find an explicit expression for the operator $\hat{X}(\pi, \sigma_t)$ that results when a Gaussian qubit pulse is applied to our dispersively coupled cavity-qubit system. That expression is indeed well-described by Eq. (S23). However, for the present discussion, we do not need to specify $\hat{X}(\pi, \sigma_t)$ beyond the description already made.

We now show the equivalence of $\hat{U}_{1,2}$ to $\hat{S}_{1,2}$ under conditions which we identify during the analysis. We begin with the qcMAP protocol \hat{U}_2 . From the definitions made, \hat{U}_2 can be rewritten as

$$\hat{U}_2 = \frac{1}{\sqrt{2}} \hat{D}(-\alpha) \hat{X}(\pi, \sigma_t) \left[\hat{D}(2\alpha)|g\rangle (\langle g| + ie^{i\phi}\langle e|) + \hat{H}|e\rangle (ie^{i\phi}\langle g| + \langle e|) \right] \quad (\text{S27})$$

from which we identify

$$\begin{aligned} \hat{S}_{gg,2} &= \frac{1}{\sqrt{2}} \hat{D}(-\alpha) \left[\langle g|\hat{X}(\pi, \sigma_t)|g\rangle \hat{D}(2\alpha) + ie^{i\phi} \hat{H} \langle g|\hat{X}(\pi, \sigma_t)|e\rangle \right] \\ &= \frac{1}{\sqrt{2}} \hat{D}(-\alpha) \left[\left(\hat{P}_{>M} + \langle g|\hat{Q}_{NM}|g\rangle \right) \hat{D}(2\alpha) + ie^{i\phi} \hat{H} \left(i\hat{P}_{\leq N} + \langle g|\hat{Q}_{NM}|e\rangle \right) \right] \end{aligned} \quad (\text{S28})$$

where we inserted Eq. (S23) to go from the first to the second line. We now wish to identify the initial states $\hat{\rho}_0$ for which $\hat{S}_{gg,2}$ fulfils Eq. (S13). Consider first an initial state $\hat{\rho}_0$ which has non-zero matrix elements only in the first N Fock states, i.e.

$$\hat{\rho}_0 = \sum_{k,l=0}^N \langle k|\hat{\rho}_0|l\rangle |k\rangle\langle l|. \quad (\text{S29})$$

For this $\hat{\rho}_0$, $\hat{P}_{\leq N}\hat{\rho}_0 = \hat{\rho}_0$. If we have additionally chosen α large enough so that the matrix element $\langle M|\hat{D}(2\alpha)|M\rangle$ is negligible, then it also follows (using the triangle inequality) that $\hat{P}_{\leq M}\hat{D}(2\alpha)\hat{\rho}_0 = 0$. In a Wigner function picture, the condition on α can be formulated as the M :th Fock state Wigner function being negligible for arguments larger than $|\alpha|$, i.e. $W_M(|\beta| \geq |\alpha|) = 0$. From $\hat{P}_{\leq N}\hat{\rho}_0 = \hat{\rho}_0$ and $\hat{P}_{\leq M}\hat{D}(2\alpha)\hat{\rho}_0 = 0$ it follows that $\hat{Q}_{NM}\hat{\rho}_0 = 0$, $\hat{Q}_{NM}\hat{D}(2\alpha)\hat{\rho}_0 = 0$, and $\hat{P}_{>M}\hat{D}(2\alpha)\hat{\rho}_0 = (1 - \hat{P}_{\leq M})\hat{D}(2\alpha)\hat{\rho}_0 = \hat{D}(2\alpha)\hat{\rho}_0$. We therefore obtain

$$\hat{S}_{gg,2}\hat{\rho}_0 = \frac{1}{\sqrt{2}} \left[\hat{D}(\alpha) - e^{i\phi} \hat{D}(-\alpha) \hat{H} \right] \hat{\rho}_0 = \hat{S}_2 \hat{\rho}_0. \quad (\text{S30})$$

The condition Eq. (S13) is also satisfied. Consequently, $\hat{U}_2\hat{\rho}_0|g\rangle\langle g|\hat{U}_2^\dagger = \hat{S}_2\hat{\rho}_0\hat{S}_2^\dagger|g\rangle\langle g|$, and \hat{S}_2 accurately describes the action of the qcMAP protocol, for all $\hat{\rho}_0$ of the form Eq. (S29) when α is such that $W_M(|\beta| \geq |\alpha|) = 0$.

Identical arguments show the equivalence of \hat{U}_1 to \hat{S}'_1 . From Eq. (S8), \hat{U}_1 can be written

$$\hat{U}_1 = \frac{1}{\sqrt{2}} \hat{D}(\alpha) \hat{X}(\pi, \sigma_t) \left[\hat{D}(-2\alpha)e^{i|\alpha|^2}|g\rangle (\langle g|ie^{i\phi} + \langle e|) - e^{-i|\alpha|^2}|e\rangle (\langle g| + ie^{-i\phi}\langle e|) \right] i^{\hat{n}}. \quad (\text{S31})$$

We identify

$$\hat{S}_{gg,1} = \frac{1}{\sqrt{2}} \hat{D}(\alpha) \left[ie^{i\phi} \left(\hat{P}_{>M} + \langle g|\hat{Q}_{NM}|g\rangle \right) \hat{D}(-2\alpha)e^{i|\alpha|^2} - e^{-i|\alpha|^2} \left(i\hat{P}_{\leq N} + \langle g|\hat{Q}_{NM}|e\rangle \right) \right] i^{\hat{n}}. \quad (\text{S32})$$

When this operator acts on a state $\hat{\rho}_0$ described by Eq. (S29), and α is large enough so that $\hat{P}_{\leq M}\hat{D}(2\alpha)\hat{\rho}_0 = 0$ as before, then

$$\hat{S}_{gg,1}\hat{\rho}_0 = \frac{-ie^{-i|\alpha|^2}}{\sqrt{2}} \left[\hat{D}(\alpha) - e^{i(\phi+2|\alpha|^2)} \hat{D}(-\alpha) \right] i^{\hat{n}} \hat{\rho}_0 = -ie^{-i|\alpha|^2} \hat{S}'_1 \hat{\rho}_0. \quad (\text{S33})$$

Eq. (S13) is satisfied. The global phase vanishes when considering $\hat{S}_{gg,1}\hat{\rho}_0\hat{S}_{gg,1}^\dagger$.

We now relax the assumption that $\hat{\rho}_0$ is of the form Eq. (S29). In general, the state after the ECD and qcMAP protocols can be written

$$\hat{U}_i\hat{\rho}_0|g\rangle\langle g|\hat{U}_i^\dagger = p_g\hat{\rho}_g|g\rangle\langle g| + p_e\hat{\rho}_e|e\rangle\langle e| + \hat{\psi} \quad (\text{S34})$$

where

$$p_g = \text{Tr} \{ \hat{S}_{gg,i}\hat{\rho}_0\hat{S}_{gg,i}^\dagger \}, \quad (\text{S35})$$

$$p_e = 1 - p_g, \quad (\text{S36})$$

are the probabilities of finding the qubit in the $|g\rangle$ and $|e\rangle$ states,

$$\hat{\rho}_g \equiv \frac{\hat{S}_{gg,i}\hat{\rho}_0\hat{S}_{gg,i}^\dagger}{p_g}, \quad (\text{S37})$$

$$\hat{\rho}_e \equiv \frac{\hat{S}_{eg,i}\hat{\rho}_0\hat{S}_{eg,i}^\dagger}{p_e} \quad (\text{S38})$$

are the qubit-conditional cavity states (where $\hat{S}_{eg,i} \equiv \langle e|\hat{U}_i|g\rangle$), and $\hat{\psi}$ represents off-diagonal terms in the qubit basis. The previous condition Eq. (S13) is $p_g = 1$. For initial states $\hat{\rho}_0$ which have non-negligible matrix elements only for Fock numbers $\leq N$, i.e. are described by Eq. (S29) plus a negligible part, one has $p_g \approx 1$, $p_e \approx 0$. More precisely, one computes

$$p_g = \frac{1}{2} \left[\langle \hat{P}_{\leq N} \rangle + \langle \hat{D}(-2\alpha)\hat{P}_{>M}\hat{D}(2\alpha) \rangle + q(\sigma_t, \alpha, n_{\text{th}}) \right] \quad (\text{S39})$$

where the expectation value is with respect to $\hat{\rho}_0$, and q represents terms related to expectation values of \hat{Q}_{NM} . If both the first two terms are 1, then $q(\sigma_t, \alpha, n_{\text{th}}) = 0$. If $\langle \hat{P}_{\leq N} \rangle \approx 1$, it is always possible to choose α such that also $\langle \hat{D}(-2\alpha)\hat{P}_{>M}\hat{D}(2\alpha) \rangle \approx 1$ and therefore $q(\sigma_t, \alpha, n_{\text{th}}) \approx 0$. For these states, the equivalence of $\hat{U}_{1,2}$ to $\hat{S}_{1,2}$ can therefore be satisfied to arbitrary precision in principle, and it is a good approximation to consider the ECD and qcMAP protocols equivalent to $\hat{S}_{1,2}$. The thermal state

$$\hat{\rho}_T \equiv \frac{1}{n_{\text{th}} + 1} \sum_{n=0}^{\infty} \left(\frac{n_{\text{th}}}{n_{\text{th}} + 1} \right)^n |n\rangle\langle n|, \quad (\text{S40})$$

is a particular example of a state which can be considered to have negligible representation for Fock numbers above N . It has

$$\text{Tr} \{ \hat{P}_{>N}\hat{\rho}_T \} = \left(\frac{n_{\text{th}}}{n_{\text{th}} + 1} \right)^{N+1} \quad (\text{S41})$$

which goes to 0 in the limit $N \rightarrow \infty$. In practice, the choice of σ_t (i.e. N and M) and α are restricted by experimental limitations, and the nonzero p_e leads to perturbations from the ideal result (i.e. that described by $\hat{S}_{1,2}$).

The conditions derived so far are those under which our protocols become equivalent to the operators $\hat{S}_{1,2}$. As a final remark, we note that one can also study the conditions for the operators $\hat{S}_{1,2}$ to be effectively unitary independently of how they are implemented. This can be done by replacing $\hat{S}_{gg,i}$ with \hat{S}_i in Eq. (S13). For a general initial state $\hat{\rho}_0$, one then has

$$\text{Tr} \{ \hat{S}_1\hat{\rho}_0\hat{S}_1^\dagger \} = 1 - \text{Re} \{ e^{-i\phi}\chi_0(2\alpha) \} = 1, \quad (\text{S42})$$

$$\text{Tr} \{ \hat{S}_2\hat{\rho}_0\hat{S}_2^\dagger \} = 1 - \frac{\pi}{2} \cos \phi W_0(\alpha) = 1. \quad (\text{S43})$$

Here, $W_0(\alpha) = 2\pi^{-1}\text{Tr} \{ \hat{H}(\alpha)\hat{\rho}_0 \}$ and $\chi_0(\alpha) = \text{Tr} \{ \hat{D}(\alpha)\hat{\rho}_0 \}$ are the Wigner and characteristic functions of the initial state. These equations can be satisfied either by choice of ϕ or α . If we want this equation to be satisfied

for any ϕ , this gives the necessary conditions that $\chi_0(|\beta| > 2|\alpha|) = 0$ (\hat{S}_1) and $W_0(|\beta| > |\alpha|) = 0$ (\hat{S}_2). We also see that if ϕ is a half-integer multiple of π , the operator \hat{S}_2 is unitary independently of α . For states that have a constant-phase characteristic function (e.g. thermal states), there are also choices of ϕ for which \hat{S}_1 is effectively unitary independently of α . To avoid confusion, we stress that ϕ does not enter any of the conditions for the ECD and qcaMAP protocols to be equivalent to the operators $\hat{S}_{1,2}$.

S2.2 Derivation of the Wigner functions $W_{1,2}(\beta)$ from the operators $\hat{S}_{1,2}$

We give derivations of the Wigner functions $W_{1,2}(\beta)$ that result when the operators $\hat{S}_{1,2}$ are applied to an initial state $\hat{\rho}_0$ and in particular the thermal state $\hat{\rho}_T$. Starting from

$$W_{1,2}(\beta) = \frac{2}{\pi} \text{Tr} \{ \hat{H}(\beta) \hat{S}_{1,2} \hat{\rho}_0 \hat{S}_{1,2}^\dagger \} \quad (\text{S44})$$

where $\hat{H}(\beta) = \hat{D}(\beta) \hat{H} \hat{D}^\dagger(\beta)$, one uses the cyclic property of the trace to express $W_{1,2}(\beta)$ as the expectation value of the operator $\hat{S}_{1,2}^\dagger \hat{H}(\beta) \hat{S}_{1,2}$ in the initial state. This allows us to express the Wigner functions $W_{1,2}(\beta)$ in terms of the Wigner function of the initial state $W_0(\beta)$, which is given by

$$W_0(\beta) = \frac{2}{\pi} \text{Tr} \{ \hat{H}(\beta) \hat{\rho}_0 \}. \quad (\text{S45})$$

Here, $\hat{\rho}_0$ is any state for which the operators $\hat{S}_{1,2}$ accurately describe the outcome of the ECD and qcaMAP protocols (see Section S2.1). One computes

$$\hat{S}_1^\dagger \hat{H}(\beta) \hat{S}_1 = \frac{1}{2} \left\{ \hat{H}(\beta - \alpha) + \hat{H}(\beta + \alpha) - 2 \cos(4\text{Im}\{\alpha^* \beta\} + \phi) \hat{H}(\beta) \right\} \quad (\text{S46})$$

and consequently

$$W_1(\beta) = \frac{1}{2} \left\{ W_0(\beta - \alpha) + W_0(\beta + \alpha) - 2 \cos(4\text{Im}\{\alpha^* \beta\} + \phi) W_0(\beta) \right\}. \quad (\text{S47})$$

If one instead of \hat{S}_1 uses \hat{S}'_1 (Eq. (S5)), the result is

$$W_{1'}(\beta) = \frac{1}{2} \left\{ W_0[-i(\beta - \alpha)] + W_0[-i(\beta + \alpha)] - 2 \cos(4\text{Im}\{\alpha^* \beta\} + \phi + 2|\alpha|^2) W_0(-i\beta) \right\}. \quad (\text{S48})$$

Further, one computes

$$\hat{S}_2^\dagger \hat{H}(\beta) \hat{S}_2 = \frac{1}{2} \left[\hat{H}(\beta - \alpha) + \hat{H}(-\beta - \alpha) - e^{i(\phi + 4\text{Im}\{\alpha^* \beta\})} \hat{D}(2\beta) - e^{-i(\phi + 4\text{Im}\{\alpha^* \beta\})} \hat{D}(-2\beta) \right] \quad (\text{S49})$$

and therefore

$$W_2(\beta) = \frac{1}{2} \left[W_0(\beta - \alpha) + W_0(-\beta - \alpha) - \frac{4}{\pi} \text{Re} \left\{ e^{i(4\text{Im}\{\alpha^* \beta\} + \phi)} \chi_0(2\beta) \right\} \right]. \quad (\text{S50})$$

Here we have identified the characteristic function [25] of the initial state

$$\chi_0(\beta) \equiv \text{Tr} \{ \hat{D}(\beta) \hat{\rho}_0 \} = \int d^2\gamma e^{2i\text{Im}\{\beta\gamma^*\}} W_0(\gamma). \quad (\text{S51})$$

Note that these Wigner functions are normalized because we have implicitly assumed an $|\alpha|$ large enough such that there is no overlap between the first two terms in each of Eqs. (S50) and (S47) (Section S2.1). For these values of $|\alpha|$, the third term in each equation oscillates rapidly enough to integrate to zero.

We now specialize to the thermal state, i.e. we set $\hat{\rho}_0 = \hat{\rho}_T$. The Wigner function of the thermal initial state is

$$W_T(\beta) = \frac{2\mathcal{P}}{\pi} e^{-2\mathcal{P}|\beta|^2} \quad (\text{S52})$$

where $\mathcal{P} = (2n_{\text{th}} + 1)^{-1}$ is the purity of the thermal state. The corresponding characteristic function is

$$\chi_T(\beta) = e^{-|\beta|^2/2\mathcal{P}}. \quad (\text{S53})$$

Replacing $W_0(\beta)$ and $\chi_T(\beta)$ in Eq. (S50) and Eq. (S47) gives

$$W_1(\beta) = \frac{\mathcal{P}}{\pi} \left[e^{-2\mathcal{P}|\beta-\alpha|^2} + e^{-2\mathcal{P}|\beta+\alpha|^2} - 2 \cos(4\text{Im}\{\alpha^*\beta\} + \phi) e^{-2\mathcal{P}|\beta|^2} \right]. \quad (\text{S54})$$

$$W_2(\beta) = \frac{1}{\pi} \left[\mathcal{P} \left(e^{-2\mathcal{P}|\beta-\alpha|^2} + e^{-2\mathcal{P}|\beta+\alpha|^2} \right) - 2 \cos(4\text{Im}\{\alpha^*\beta\} + \phi) e^{-2|\beta|^2/\mathcal{P}} \right]. \quad (\text{S55})$$

These are the Wigner functions given in the main text up to a redefinition of the parameter ϕ ($\phi \rightarrow \phi + \pi$). Eq. (S54) is also obtained from $W'_1(\beta)$ if one inserts the thermal Wigner function and redefines ϕ to absorb the geometric phase.

S2.3 Hot cat state coherence functions

In this section, we give the full two-dimensional hot cat coherence functions as well as their derivations. As stated in the main text, the first-order coherence function of a quantum state with density matrix $\hat{\rho}$ is defined as

$$g(x_1, x_2) \equiv \frac{|\langle x_1 | \hat{\rho} | x_2 \rangle|}{\sqrt{\langle x_1 | \hat{\rho} | x_1 \rangle \langle x_2 | \hat{\rho} | x_2 \rangle}}. \quad (\text{S56})$$

Here $x_{1,2}$ are real-valued dimensionless numbers, and $|x_{1,2}\rangle$ are eigenkets of the quadrature operator

$$\hat{x} \equiv \frac{\hat{c} + \hat{c}^\dagger}{\sqrt{2}}, \quad (\text{S57})$$

meaning that $\hat{x}|x_1\rangle = x_1|x_1\rangle$ and equivalently for x_2 . Due to the positive semidefiniteness of $\hat{\rho}$, the coherence function is bounded: $1 \geq g(x_1, x_2) \geq 0$.

We compute the coherence function from $W_{1,2}(\beta)$ using the relation

$$\langle x_1 | \hat{\rho} | x_2 \rangle = \frac{1}{2} \int_{-\infty}^{\infty} dp W \left(\frac{x_1 + x_2}{2\sqrt{2}} + \frac{ip}{\sqrt{2}} \right) e^{ip(x_1 - x_2)} \quad (\text{S58})$$

which can be derived e.g. from the expression for computing expectation values from the Wigner function $\langle \hat{A} \rangle = \text{Tr}\{\hat{A}\hat{\rho}\} = \int d^2\gamma 2\text{Tr}\{\hat{H}(\gamma)\hat{A}\}W(\gamma)$ with $\hat{A} = |x_2\rangle\langle x_1|$. It is helpful to first remind ourselves of the coherence function of a thermal state. Using Eq. (S52) in Eq. (S58), we find the coherence function

$$g_T(x_1, x_2) \equiv \exp \left\{ -\frac{(x_1 - x_2)^2 (1 - \mathcal{P}^2)}{4\mathcal{P}} \right\} \quad (\text{S59})$$

which we denote g_T since it is the coherence function of the thermal state $\hat{\rho}_T$. The thermal state coherence function is independent of the position on the diagonal $x_1 + x_2$ and is a Gaussian in the distance from the diagonal $x_1 - x_2$. Its standard deviation

$$\xi_{\text{th}} \equiv \sqrt{\frac{2\mathcal{P}}{1 - \mathcal{P}^2}}. \quad (\text{S60})$$

is termed the coherence length. When $\mathcal{P}^2 \ll 1$, $\xi_{\text{th}} \approx \sqrt{2\mathcal{P}}$. In this case, the coherence length is related to the quadrature standard deviation of the thermal state $\sigma_x \equiv \sqrt{\text{Tr}\{\hat{x}^2 \hat{\rho}_0\}} = 1/\sqrt{2\mathcal{P}}$ by the reciprocal relationship $\xi_{\text{th}} = 1/\sigma_x$. In the opposite limit, $\mathcal{P} \rightarrow 1$, $\xi_{\text{th}} \rightarrow \infty$ since in this case $g(x_1, x_2) \rightarrow 1$.

We denote the coherence functions of the ECD and qcMAP states respectively as $g_1(x_1, x_2)$ and $g_2(x_1, x_2)$. We also introduce the notation $\bar{x} \equiv (x_1 + x_2)/2$ and $\Delta x \equiv x_1 - x_2$ to make expressions more concise. From Eq. (S56), Eq. (S58) and Eqs. (S55) and (S54), we compute

$$g_1(x_1, x_2) = \frac{e^{-(\Delta x)^2/2\xi_{\text{th}}^2} \left| \cosh(\sqrt{2\alpha\mathcal{P}2\bar{x}}) - e^{-4\alpha^2/\xi_{\text{th}}^2} \cosh(\sqrt{2\alpha\Delta x/\mathcal{P}} - i\phi) \right|}{\sqrt{[\cosh(2\sqrt{2\alpha\mathcal{P}}x_1) - e^{-4\alpha^2/\xi_{\text{th}}^2} \cos(\phi)] [\cosh(2\sqrt{2\alpha\mathcal{P}}x_2) - e^{-4\alpha^2/\xi_{\text{th}}^2} \cos(\phi)]}}. \quad (\text{S61})$$

and

$$g_2(x_1, x_2) = \frac{\left| e^{-(\Delta x)^2/2\xi_{\text{th}}^2} \cosh(\sqrt{2\alpha\mathcal{P}2\bar{x}}) - e^{-(2\bar{x})^2/2\xi_{\text{th}}^2} \cosh(\sqrt{2\alpha\mathcal{P}\Delta x} - i\phi) \right|}{\sqrt{[\cosh(2\sqrt{2\alpha\mathcal{P}}x_1) - e^{-2x_1^2/\xi_{\text{th}}^2} \cos(\phi)] [\cosh(2\sqrt{2\alpha\mathcal{P}}x_2) - e^{-2x_2^2/\xi_{\text{th}}^2} \cos(\phi)]}}. \quad (\text{S62})$$

These expressions are exact, and we plot them as 2-dimensional functions of x_1 and x_2 in Figure S5. In the remainder of this section, we will explain the appearance of Figure S5 by making approximations.

We are mainly interested in understanding $g_{1,2}$ for $\mathcal{P} \ll 1$ and for (x_1, x_2) away from the origin $(0, 0)$ (since our nonzero entries in $\langle x_1 | \hat{\rho} | x_2 \rangle$ are centered around the four points $(\pm\sqrt{2\alpha}, \pm\sqrt{2\alpha})$, $(\pm\sqrt{2\alpha}, \mp\sqrt{2\alpha})$, and we must have $\alpha > \sigma_x = 1/\sqrt{2\mathcal{P}}$). When the purity is not close to 1, the terms $\propto \cos(\phi)$ in the denominators of $g_{1,2}$ are generally negligible (g_1) or nonzero only close to the coordinate axes (g_2). We therefore drop these terms, which makes the denominators of $g_{1,2}$ equal. Using the hyperbolic trig relations, we rewrite the denominators to be $[\cosh(2\sqrt{2\alpha\mathcal{P}2\bar{x}}) + \cosh(2\sqrt{2\alpha\mathcal{P}\Delta x})]/2$. Finally, we approximate $\cosh(x) \approx \exp(|x|)/2$ for both \bar{x} and Δx . This gives

$$g_1(x_1, x_2) \approx \frac{\exp\{-(\Delta x)^2/2\xi_{\text{th}}^2\}}{\sqrt{1 + \exp\{2\sqrt{2\alpha\mathcal{P}}(|\Delta x| - 2|\bar{x}|\)}}} + \frac{\exp\{-(|\Delta x| - 2\sqrt{2\alpha})^2/2\xi_{\text{th}}^2\}}{\sqrt{1 + \exp\{2\sqrt{2\alpha\mathcal{P}}(2|\bar{x}| - |\Delta x|)\}}}. \quad (\text{S63})$$

$$g_2(x_1, x_2) \approx \frac{\exp\{-(\Delta x)^2/2\xi_{\text{th}}^2\}}{\sqrt{1 + \exp\{2\sqrt{2\alpha\mathcal{P}}(|\Delta x| - 2|\bar{x}|\)}}} + \frac{\exp\{-(2\bar{x})^2/2\xi_{\text{th}}^2\}}{\sqrt{1 + \exp\{2\sqrt{2\alpha\mathcal{P}}(2|\bar{x}| - |\Delta x|)\}}}, \quad (\text{S64})$$

These expressions differ only in the nominator of the last term. The denominators are approximately indicator functions for the $x_1 x_2 > 0$ quadrants (first term denominator) and $x_1 x_2 < 0$ quadrants (second term denominator) of the (x_1, x_2) plane, i.e.

$$\frac{1}{\sqrt{1 + \exp\{2\sqrt{2\alpha\mathcal{P}}(|\Delta x| - 2|\bar{x}|\)}}} \approx [x_1 x_2 > 0] = \begin{cases} 1 & x_1 x_2 > 0 \\ 0 & x_1 x_2 < 0 \end{cases}, \quad (\text{S65})$$

$$\frac{1}{\sqrt{1 + \exp\{2\sqrt{2\alpha\mathcal{P}}(2|\bar{x}| - |\Delta x|)\}}} \approx [x_1 x_2 < 0] = \begin{cases} 0 & x_1 x_2 > 0 \\ 1 & x_1 x_2 < 0 \end{cases}. \quad (\text{S66})$$

(The notation $[\]$ for the conditional expressions is called the Iverson bracket). Using this observation, we arrive at our final expressions for $g_{1,2}$:

$$g_1(x_1, x_2) \approx g_T(x_1, x_2)[x_1 x_2 > 0] + g_T(|x_1 - x_2|, 2\sqrt{2\alpha})[x_1 x_2 < 0]. \quad (\text{S67})$$

$$g_2(x_1, x_2) \approx g_T(|x_1|, |x_2|). \quad (\text{S68})$$

When $\mathcal{P} \ll 1$, the approximation Eq. (S65) loses accuracy in Eq. (S63), and in this limit we should instead replace $[x_1 x_2 > 0]$ by 1 in Eq. (S67) to get an accurate approximation for $g_1(x_1, x_2)$. Eqs. (S67) and (S68) agree well with the exact functions plotted in Figure S5.

Along the line $l(s) \equiv (x_1(s), x_2(s)) = \sqrt{2}\alpha(2s - 1, -1)$, $s \in [0, \infty]$ in the (x_1, x_2) plane, g_1 and g_2 are equal within our approximations leading up to Eqs. (S67) and (S68). This is the line along which we plot the hot cat state coherence functions in Figure 1C in the main text.

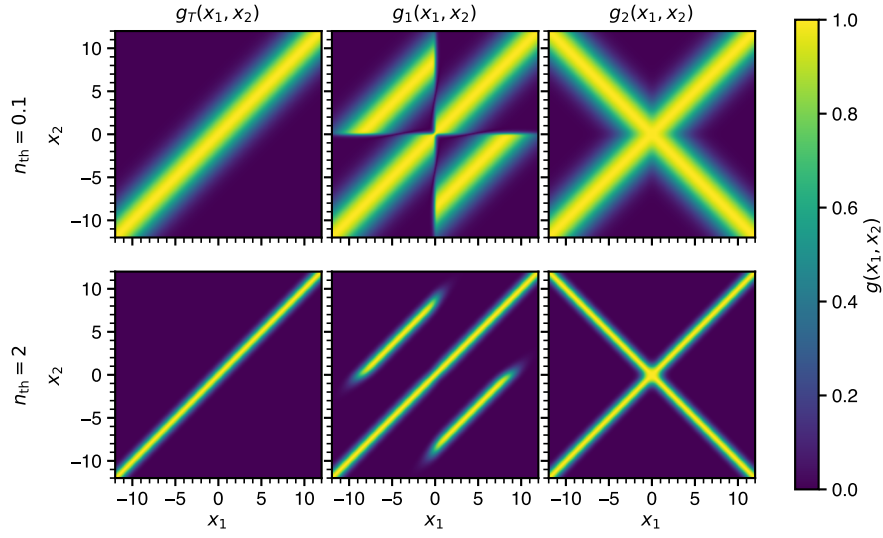


Fig. S5. Hot Schrödinger Cat State Coherence Functions. Shown is the thermal state coherence function $g_T(x_1, x_2)$ Eq. (S59) (left column), and the two cat coherence functions $g_1(x_1, x_2)$ Eq. (S61) (center column) and $g_2(x_1, x_2)$ Eq. (S62) (right column) for a cold (top row) and hot (bottom row) n_{th} . The plot uses $\alpha = 3$ and $\phi = 0$.

S3 Numerical model

Based on our characterization of the experimental setup, we introduce the numerical *ab initio* model of our experiment and compare its predictions to the experimentally measured data.

S3.1 Method

We perform all numerical work using QuTiP version 4.7 [45]. We simulate the ECD and qcMAP protocols as follows: Displacement operators and thermal initial states are implemented using QuTiP's built-in functions. The time evolution operations $\hat{T}(t)$ are implemented using QuTiP's built-in functions to simulate the cavity-qubit dynamics during time evolution, as described in the next paragraph. The qubit and cavity-conditional qubit operations are implemented by simulating the qubit-cavity dynamics under a driving Hamiltonian, as described in more detail below. This lets us compute the density matrix resulting from the state preparation protocols. We obtain the result of the Wigner function measurement from this density matrix by computing the expectation value of the observable

$$\hat{M}(\beta) \equiv \frac{2}{\pi} \hat{\Pi}(\beta) (|g\rangle\langle g| - |e\rangle\langle e|). \quad (\text{S69})$$

This observable gives the outcome of the Wigner function measurement when decoherence and nonlinearities during the measurement sequence are neglected [15].

We simulate the time-evolution operators $\hat{T}(t)$ by using QuTiP's built-in `mesolve` function to solve the following Lindblad equation

$$\frac{\partial}{\partial t} \hat{\rho}(t) = \mathcal{L} \hat{\rho}(t) \equiv -\frac{i}{\hbar} [\hat{H}, \hat{\rho}(t)] + \left(\gamma_1 \mathcal{D}[|g\rangle\langle e|] + \frac{\gamma_2}{2} \mathcal{D}[\hat{\sigma}_z] + \Gamma \mathcal{D}[\hat{c}] \right) \hat{\rho}(t) \quad (\text{S70})$$

from $t = t_0$, where $\hat{\rho}(t_0)$ is the total cavity-qubit state before the \hat{T} operation is to be applied, until the final time t . The state $\hat{\rho}(t)$ is then used as input for the next step of the protocol. Here $\gamma_1 = 1/T_1$, $\gamma_2 = 1/T_2^*$ are the dissipation and dephasing rates of the qubit and $\Gamma = 1/T_{1,c}$ is the dissipation rate of the cavity. \mathcal{D} is the dissipator superoperator, defined as

$$\mathcal{D}[\hat{A}] \hat{\rho}(t) \equiv \hat{A} \hat{\rho}(t) \hat{A}^\dagger - \frac{1}{2} \left(\hat{A}^\dagger \hat{A} \hat{\rho}(t) + \hat{\rho}(t) \hat{A}^\dagger \hat{A} \right), \quad (\text{S71})$$

for an arbitrary operator \hat{A} , and \hat{H} is the Hamiltonian in the interaction picture of the cavity and qubit including the dominant higher-order perturbations

$$\frac{1}{\hbar} \hat{H} \equiv -\chi_{\text{qc}} \hat{c}^\dagger \hat{c} |e\rangle\langle e| - \left(\frac{K_c}{2} + \frac{\chi'_{\text{qc}}}{2} |e\rangle\langle e| \right) \hat{c}^\dagger \hat{c}^\dagger \hat{c} \hat{c}. \quad (\text{S72})$$

We choose the parameters $K_c, \chi'_{\text{qc}}, \gamma_1, \gamma_2, \Gamma$ to be the values measured in the experiment (Table S1).

For the qubit operations, we use QuTiP's built-in `mesolve` function to solve the Lindblad equation

$$\frac{\partial}{\partial t} \hat{\rho}(t) = \mathcal{L} \hat{\rho}(t) - \frac{i}{\hbar} [\hat{H}_{\text{drive}}, \hat{\rho}(t)] \quad (\text{S73})$$

from time t_0 , where $\hat{\rho}(t_0)$ is the total cavity-qubit state before the qubit operation is applied, to time t , when the next operation is applied, and we use $\hat{\rho}(t)$ as initial state for the following operation. The driving Hamiltonian is

$$\frac{1}{\hbar} \hat{H}_{\text{drive}} \equiv \frac{\Omega(t)}{2} (e^{i\phi} |e\rangle\langle g| + e^{-i\phi} |g\rangle\langle e|) \quad (\text{S74})$$

with

$$\Omega(t) \equiv \frac{\theta e^{-(t-t_0-T/2)^2/2\sigma_t^2}}{\sqrt{2\pi\sigma_t^2} \operatorname{erf}(T/2^{3/2}\sigma_t)}. \quad (\text{S75})$$

Here T is the pulse duration so that $t = T + t_0$, erf is the error function, and θ is the pulse area over the interval T :

$$\int_{t_0}^{t_0+T} d\tau \Omega(\tau) = \theta. \quad (\text{S76})$$

We use $T = 4\sigma_t$ as this is the value used in the experiment. We take θ , σ_t and ϕ as the parameters of the pulse and choose them according to the desired operation to be modelled. In particular, $\sigma_t = 6$ ns for the global qubit operations, and $\sigma_t = 20$ ns for the cavity-selective disentanglement pulse. We compensate the free evolution times for the finite length of the qubit pulses, so that the maximum of the disentanglement pulse occurs at $t = \pi/\chi_{\text{qc}}$ in both protocols, and in the ECD protocol, the maximum of the qubit echo pulse occurs at $t = \pi/2\chi_{\text{qc}}$.

S3.2 Comparison of Simulation and Data

We run our simulations with all parameters of the Lindbladian taking the values that we measure experimentally (Table S1), and the pulse parameters being the experimentally used values. We present a comparison of the simulation results to the experimental Wigner map data in Figure S7. Here we simulated with $n_{\text{th}} = 3.48$, $\alpha = 3.06$ for the ECD protocol and $\alpha = 3.47$ for the ECD protocol, and $\phi = \pi$. To facilitate a comparison of the simulations to the data, we displace the simulated Wigner functions so that their fringe pattern aligns with that of the data. We do this by identifying the coherence fringe in the simulated Wigner functions corresponding most closely to the coherence fringe centered at $\beta = 0$ in the data. We then displace the simulated Wigner functions so that the identified fringe is also centered at $\beta = 0$. Specifically, the simulated ECD Wigner function was displaced by $0.654i$ and the simulated qcMAP Wigner function was displaced by $0.111 - 0.353i$. We additionally rotate the qcMAP state clockwise by 0.163 radians so that the centers of the displaced thermal states lie along the $\text{Re}\{\beta\}$ axis. The ECD state was not rotated.

Using the same simulation parameters as for the Wigner maps (including the final displacement and rotations), we also simulate the Wigner function linecuts along the $\text{Re}\{\beta\}$ and $\text{Im}\{\beta\}$ axes for the values of n_{th} that were reported in Figure 2D-G. We present the computed linecuts in Figure S8.

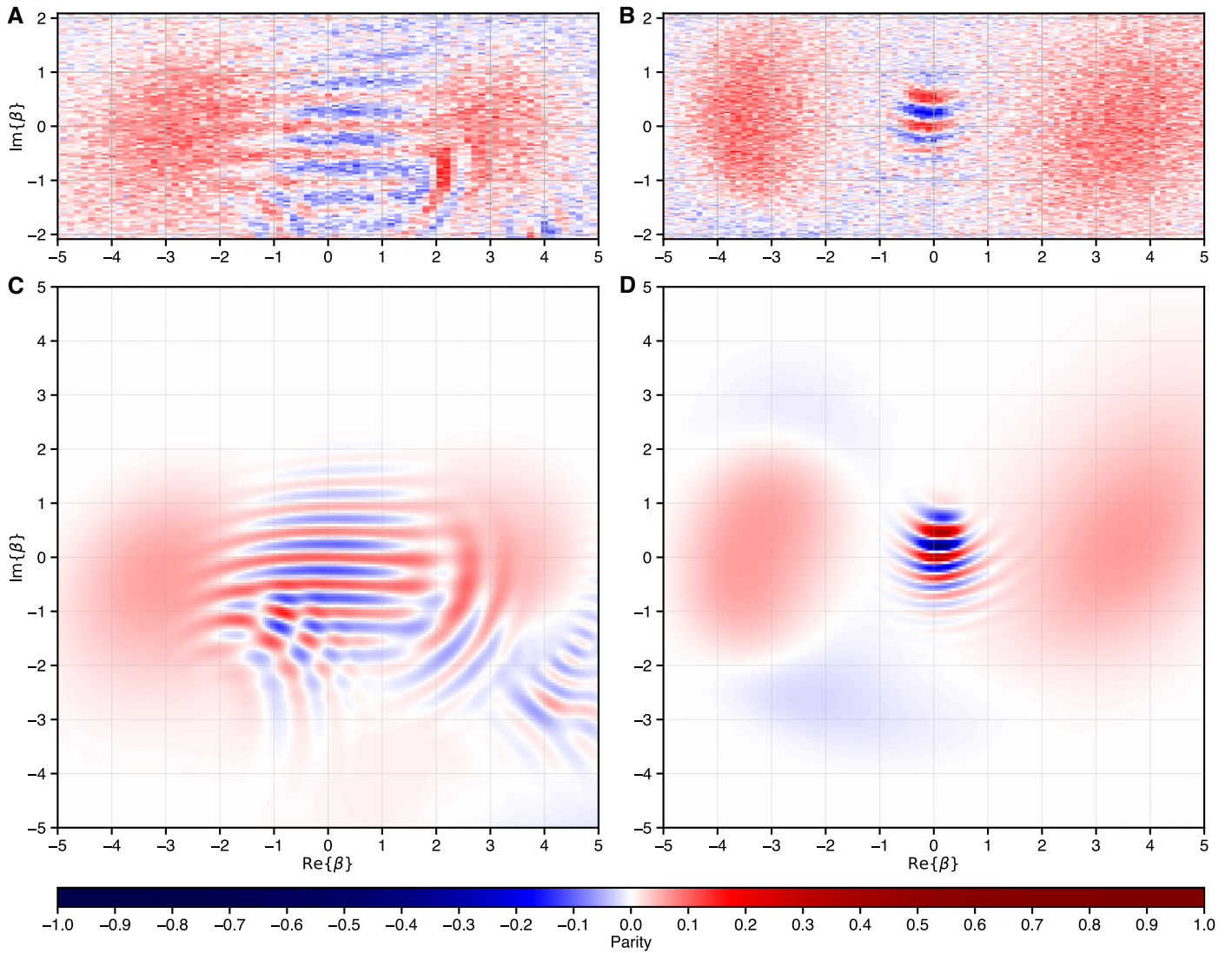


Fig. S7. Comparison of simulated Wigner maps to measured data. (A) Experimental data obtained for the ECD protocol (also displayed in Figure 1B). (B) Experimental data obtained for the qcMAP protocol (also displayed in Figure 1C). (C) Result of the numerical simulation of the ECD protocol. (D) Result of the numerical simulation of the qcMAP protocol.

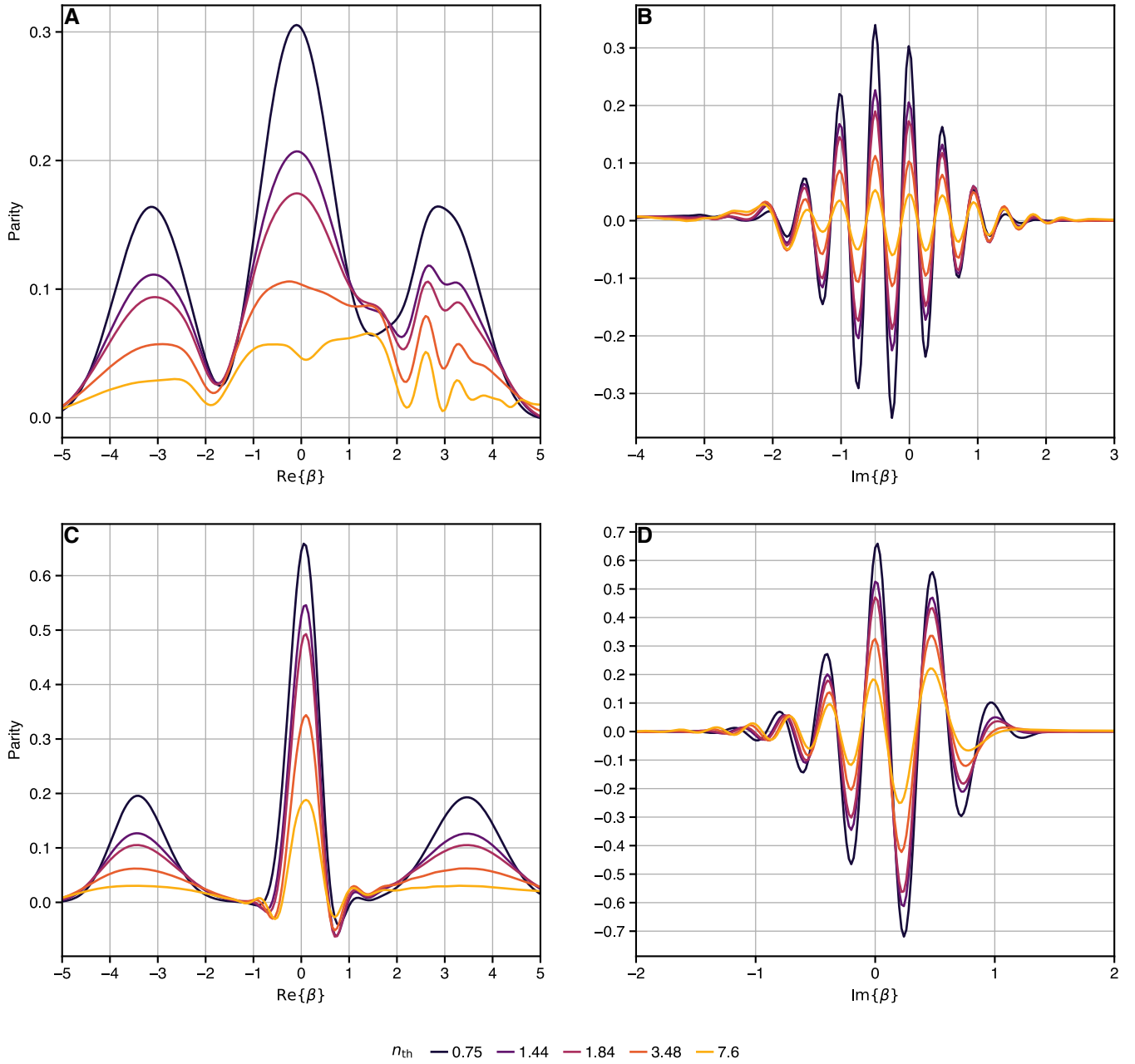


Fig. S8. Wigner function linecuts obtained from simulation. The line colors are chosen in analogy to the line colors in Figure 1D-G. (A) Linecut along $\text{Re}\{\beta\}$ through the ECD Wigner function. (B) Linecut along $\text{Im}\{\beta\}$ through the ECD Wigner function. (C) Linecut along $\text{Re}\{\beta\}$ through the qcMAP Wigner function. (D) Linecut along $\text{Im}\{\beta\}$ through the qcMAP Wigner function.

S4 Analysis of Imperfections

The experimentally achieved protocols differ from the ideal ECD and qcMAP protocols analyzed theoretically in Section S2. In this section, we study the identified differences in isolation using a combination of analytical and numerical methods. By comparing the results to the ideal protocols and the data, we can attribute features in the data which are not seen in the theoretical Wigner functions to particular experimental imperfections.

S4.1 Residual cavity-qubit entanglement

The experimental imperfections lead to a finite probability p_e of the qubit being in the excited state at the end of the protocol. From Eq. (S69) and Eq. (S34), one computes that the expected result of the measurement is

$$W_{\text{meas.}}(\beta) \equiv \text{Tr} \left\{ \hat{M}(\beta) \hat{U} \hat{\rho}_0 |g\rangle\langle g| \hat{U}^\dagger \right\} = p_g W_g(\beta) - p_e W_e(\beta). \quad (\text{S77})$$

Here, we have introduced the qubit-conditional Wigner functions

$$W_{g,e}(\beta) \equiv \frac{2}{\pi} \text{Tr} \{ \hat{H}(\beta) \hat{\rho}_{g,e} \}. \quad (\text{S78})$$

Imperfect disentanglement between the cavity and qubit will lead to $p_e > 0$, $p_g < 1$. In this case, the output of the Wigner function measurement is not the final state Wigner function, but rather the weighted difference of the Wigner functions of the qubit-conditional states $\hat{\rho}_g$ and $\hat{\rho}_e$, with the weights being p_g and p_e . As long as $p_g \gg p_e$ and/or the Wigner functions $W_g(\beta)$ and $W_e(\beta)$ do not overlap significantly, the residual qubit-cavity entanglement is a perturbative imperfection to measurement of the final cavity state Wigner function.

S4.2 Comparison of simulations with different parameters

To understand the effect of each difference between our experiment and the ideal ECD and qcMAP protocols, we run our simulations with different sets of parameters which are chosen to isolate each difference. We present the results of these simulations in Figures S9 (ECD) and S10 (qcMAP). We go through the parameters used for each panel of these figures in the next paragraphs.

‘Experimental parameters’ (panel A) refers to the simulations as described in Section S3, where we chose the parameters to match the experiment as closely as possible (however, in Figures S9 and S10, we do not rotate or displace the Wigner functions before plotting).

‘Reference parameters’ (panel B) refers to a set of parameters chosen to match the ideal ECD and qcMAP protocols considered in Section S2.1. These simulations have no Kerr nonlinearities, negligible width of the non-selective qubit pulses, infinite coherence times, and a disentanglement pulse width which was optimized by sweeping σ_t for these parameters and choosing the σ_t that minimized p_e in this scenario. Specifically, the reference parameters are: $K_c = \chi'_{\text{qc}} = 0$, $\Gamma = \gamma_1 = \gamma_2 = 0$, disentanglement pulse $\sigma_t = 6$ ns, other qubit pulses $\sigma_t = 10^{-13}$ s.

Panels C-F show simulations using the reference parameters but with a subset of the parameters set to their experimental values, as explained in the figure captions.

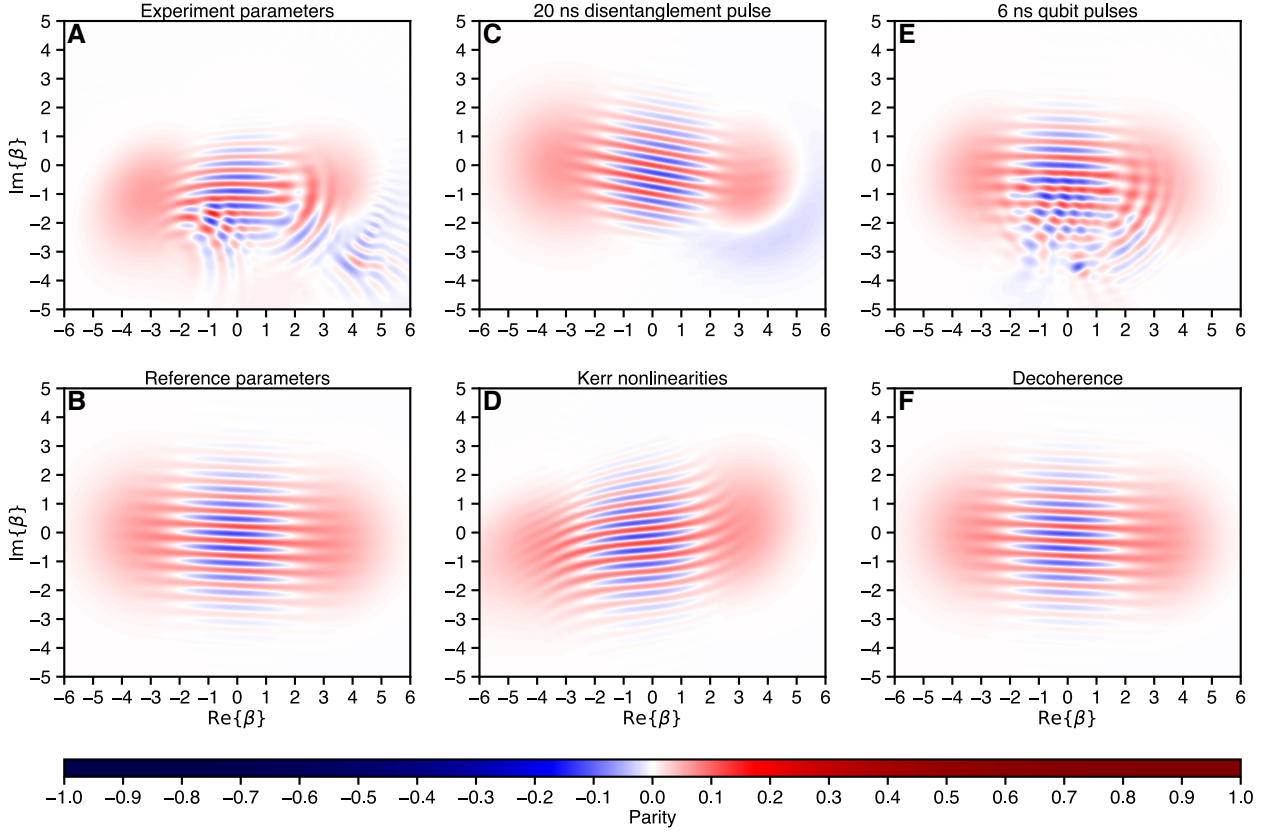


Fig. S9. Comparison of simulations with different parameters for ECD. We simulate the hot cat state preparation protocols with different sets of parameters, which are chosen to isolate the differences between our experiment and the ideal ECD protocol. All simulations shown used $n_{\text{th}} = 3.48$ and $\alpha = 3.06$. **(A)** Simulation with all parameters taking the values measured or used in the experiment, as in Fig. S7C. **(B)** Simulation with parameters chosen to match the ideal ECD protocol (see Section S4.2). **(C)** Simulation with the reference parameters but the disentanglement pulse standard deviation σ_t set to the experiment value of 20 ns. **(D)** Simulation with the reference parameters but the Kerr nonlinearity parameters K_c and χ'_{qc} taking their experimentally measured values. **(E)** Simulation with the reference parameters but the σ_t of all qubit pulses set to 6 ns, the minimum pulse σ_t that our experimental instrumentation can achieve. **(F)** Simulation with the reference parameters but with the coherence times T_1 , T_2^* and $T_{1,c}$ taking their experimental values.

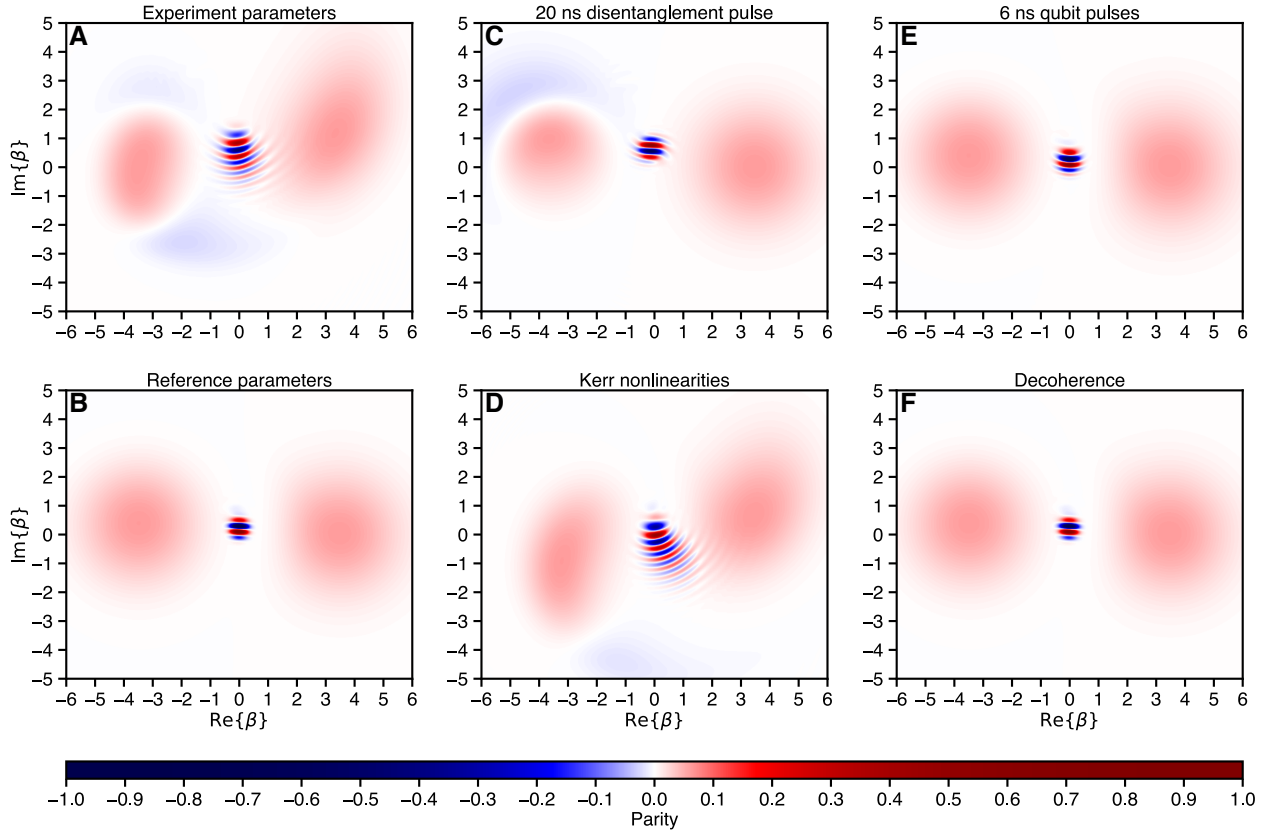


Fig. S10. Comparison of simulations with different parameters for qcMAP. We simulate the hot cat state preparation protocols with different sets of parameters, which are chosen to isolate the differences between our experiment and the ideal qcMAP protocol. All simulations shown used $n_{\text{th}} = 3.48$ and $\alpha = 3.47$. **(A)** Simulation with all parameters taking the values measured or used in the experiment, as in Fig. S7D. **(B)** Simulation with parameters chosen to match the ideal qcMAP protocol (see Section S4.2). **(C)** Simulation with the reference parameters but the disentanglement pulse standard deviation σ_t set to the experiment value of 20 ns. **(D)** Simulation with the reference parameters but the Kerr nonlinearity parameters K_c and χ'_{qc} taking their experimentally measured values. **(E)** Simulation with the reference parameters but the σ_t of all qubit pulses set to 6 ns, the minimum pulse σ_t that our experimental instrumentation can achieve. **(F)** Simulation with the reference parameters but with the coherence times T_1 , T_2^* and $T_{1,c}$ taking their experimental values.

S4.3 Free evolution timing errors

In the experiment, all cavity and qubit operation pulses take a finite time. Cavity displacement pulses take 16 ns, and qubit operations take $4\sigma_t$ to complete (24 ns for non-selective qubit pulses, 80 ns for the disentanglement pulse). The design of the experimental protocol takes this into account by optimizing the pulse timings, with a step size of 4 ns. Nevertheless, here we theoretically investigate the effects of perturbing the time argument of the free evolution operator $\hat{T}(t)$ in the qcMAP protocol. We show that such perturbations, if present, lead to bending distortions of the hot cat state fringes which are not seen for cold cat states.

In the ideal qcMAP protocol, the free evolution time is π/χ_{qc} . Here we take the free evolution time to be $\pi/\chi_{\text{qc}} + \tau$, where τ is the timing error. Following the analysis in Section S2.1, the effective operator of the protocol becomes

$$\hat{S}_1 = \frac{1}{\sqrt{2}} \left[1 - \exp \{i(\chi_{\text{qc}}\tau\hat{n} + \phi)\} \hat{H} \right] \hat{D}(\alpha). \quad (\text{S79})$$

The Wigner function resulting from the application of this operator on a cavity state can be computed using the same methods as in Section S2.2. The result is

$$W_1(\beta) = \frac{1}{2} \left[W_0(\beta - \alpha) + W_0(-\alpha - \beta e^{-i\chi_{\text{qc}}\tau}) - \frac{4}{\pi} \text{Re} \left\{ e^{i\varphi} \text{Tr} \left\{ \hat{D} [2\beta + \alpha(e^{i\chi_{\text{qc}}\tau} - 1)] \exp \{i\chi_{\text{qc}}\tau\hat{n}\} \hat{\rho}_0 \right\} \right\} \right] \quad (\text{S80})$$

with

$$\varphi = \phi + 2\text{Im} \{ \alpha^* \beta [1 + \exp(-i\chi_{\text{qc}}\tau)] \} + |\alpha|^2 \sin(\chi_{\text{qc}}\tau). \quad (\text{S81})$$

For a thermal state $\hat{\rho}_0 = \hat{\rho}_T$,

$$\begin{aligned} \text{Tr} \left\{ \hat{D} [2\beta + \alpha(e^{i\chi_{\text{qc}}\tau} - 1)] \exp \{i\chi_{\text{qc}}\tau\hat{n}\} \hat{\rho}_0 \right\} &= \\ &= \frac{1}{1 + n_{\text{th}}(1 - e^{i\chi_{\text{qc}}\tau})} \exp \left\{ - \left(\frac{1}{2} + \frac{n_{\text{th}} e^{i\chi_{\text{qc}}\tau}}{1 + n_{\text{th}}(1 - e^{i\chi_{\text{qc}}\tau})} \right) |2\beta + \alpha(e^{i\chi_{\text{qc}}\tau} - 1)|^2 \right\}. \end{aligned} \quad (\text{S82})$$

Taking $\tau = 0$ recovers Eq. (S55) as expected. To understand the effect of a small τ , we linearize Eq. (S81) and Eq. (S82) in τ . Taking α to be real, the coherence term in Eq. (S80) linearized in τ is

$$\begin{aligned} \frac{4}{\pi} \cos \{ 4\alpha \text{Re} \{ k^* \beta \} + \phi' + 4\chi_{\text{qc}}\tau |\beta|^2 n_{\text{th}} (1 + n_{\text{th}}) \} \\ \cdot \exp \{ -2(2n_{\text{th}} + 1) (|\beta|^2 + \chi_{\text{qc}}\tau \alpha \text{Im} \{ \beta \}) \}. \end{aligned} \quad (\text{S83})$$

Here $k \equiv -\chi_{\text{qc}}\tau/2 + i$ and $\phi' \equiv \phi + \chi_{\text{qc}}\tau(|\alpha|^2 + n_{\text{th}})$. This expression contains three additional effects compared to the $\tau = 0$ case: 1) The phase shift has changed from ϕ to ϕ' . 2) Since the left Gaussian has moved in the $\text{Im} \{ \beta \}$ direction, the center of the fringes has also moved in the $\text{Im} \{ \beta \}$ direction, and k has obtained a real part. 3) The presence of $|\beta|^2$ in the cosine argument causes a bending distortion of the fringes. The $|\beta|^2$ term vanishes when $n_{\text{th}} \rightarrow 0$, so that noticeable bending of the fringes occurs only for hot cats.

For illustration, we plot Eq. (S80) in Figure S11 for $\alpha = 3.47$, $n_{\text{th}} = 3.48$, $\phi = \pi$, and a timing error of $\tau = 20$ ns. We emphasize that this value of τ is much larger than the 4 ns steps with which we optimize the pulse timings in our experiment. Figure S11 bears some resemblance to Figures S7 and S8; however, our numerical simulations do not contain any timing error, and the fringe bending observed in our experiment is mainly due to the Kerr nonlinearity (see Section S4.2).

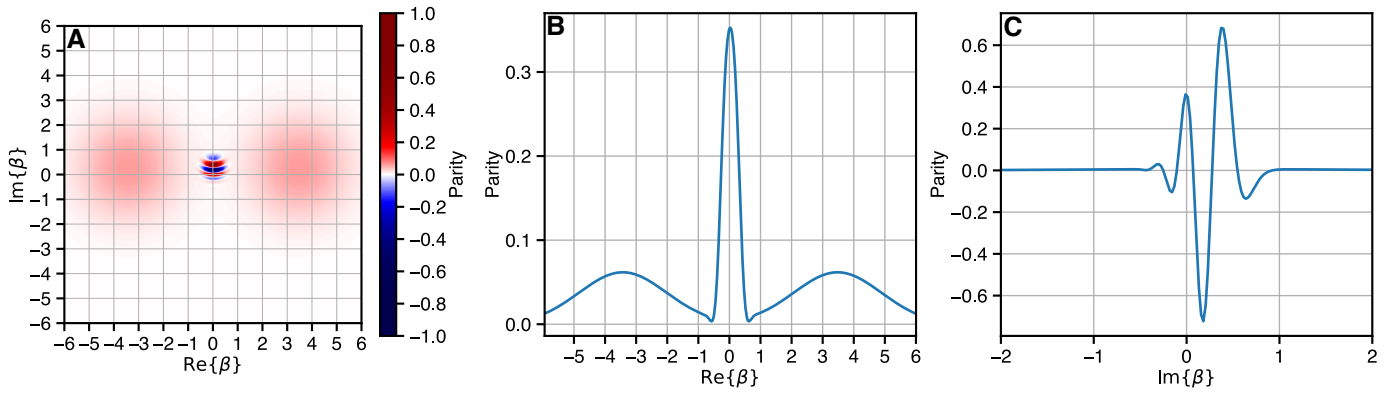


Fig. S11. Fringe bending due to timing errors. (A) Wigner function Eq. (S80) for a timing error of 20 ns. The Wigner function has been rotated and displaced before plotting to remove the extra rotation due to the timing error and center the fringe pattern at $\beta = 0$. (B) Linecut through the Wigner function in panel A along $\text{Re}\beta$. (C) Linecut through the Wigner function in panel A along $\text{Im}\beta$.